

# 1 **Fast uplift in the Southern Patagonian Andes due to long and** 2 **short term deglaciation and the asthenospheric window** 3 **underneath**

4  
5 Veleda A. P. Muller<sup>1</sup>, Pietro Sternai<sup>1</sup>, Christian Sue<sup>2,3</sup>

6 <sup>1</sup> Dipartimento di Scienze dell'Ambiente e della Terra (DISAT), Università degli Studi di  
7 Milano-Bicocca, Piazza della Scienza 4, Milan, Italy

8 <sup>2</sup> Institute des Sciences de la Terre (ISterre), Université Grenoble Alpes, Université Savoie  
9 Mont Blanc, CNRS, IRD, IFSTTAR, Université Gustave Eiffel, Grenoble, France.

10 <sup>3</sup> Université de Franche Comté, Besançon, France.

11 *Correspondence to:* Veleda A.P. Muller (v.paivamuller@campus.unimib.it)

12  
13  
14 **Abstract.** An asthenospheric window underneath much of the South American continent  
15 increases the heat flow in the Southern Patagonian Andes, where glacial-interglacial cycles  
16 drive the building and melting of the Patagonian Icefields since the latest Miocene. The Last  
17 Glacial Maximum (LGM) was reached ~26000 years Before Present (BP). Significant  
18 deglaciation onsets between 21000 and 17000 years BP, subject to an acceleration since the  
19 Little Ice Age (LIA), ~400 years BP. Fast uplift rates of up to  $41 \pm 3$  mm/yr are measured by  
20 GNSS around the Southern Patagonian Icefield and currently ascribed to post-LIA  
21 lithospheric rebound, but the possible longer-term post-LGM rebound is poorly constrained.  
22 These uplift rates, in addition, are one order of magnitude higher than those measured on  
23 other glaciated orogens (e.g., the European Alps), which raises questions about the role of the  
24 asthenospheric window in affecting the vertical surface displacement rates. Here, we perform  
25 geodynamic thermo-mechanical numerical modelling to estimate the surface uplift rates  
26 induced by post-LIA and post-LGM deglaciation accounting for temperature dependent  
27 rheologies and different thermal regimes in the asthenosphere. Our modelled maximum  
28 postglacial rebound matches the observed uplift rate budget only when both post-LIA and  
29 post-LGM deglaciation are accounted for and if a standard continental asthenospheric mantle  
30 potential temperature is increased by 150-200 °C. The asthenospheric window thus plays a  
31 key role in controlling the magnitude of presently observed uplift rates in the Southern  
32 Patagonian Andes.

## 1. Introduction

Vertical displacements of the Earth's surface with respect to the geoid occur in response to the motion of crustal and mantle rock masses due to [mantle dynamics](#), plate tectonics, and the redistribution of sediments, water, and ice by surface processes (e.g., Molnar and England, 1990; Watts, 2001; Champagnac et al., 2012; Sternai, 2023; Cloetingh et al., 2023). For instance, excess of topography in orogenic regions due to convergence, [crustal shortening, and magmatism](#) deflects the lithosphere downward, whereas [surface unloading](#) by erosion and ice melting causes upward deflection of the lithosphere, known as “isostatic” adjustment (e.g., Peltier and Andrews, 1976; Peltier, 1996, 2004; Mitrovica and Forte, 1997; Butler and Peltier, 2000; Kaufman and Lambeck, 2002; Watts, 2001; Turcotte and Schubert, 2002; Sternai et al., 2016a). [Glacial isostatic adjustment \(GIA\) models study the visco-elastic response of the solid Earth to the building and melting of regional ice sheets and commonly use GNSS and/or satellite-measured rock uplift rates in regions subject to deglaciation to estimate, for instance, the regional mantle rheology and sea-level changes \(e.g., Peltier and Andrews, 1976; Peltier, 1996, 2004; Mitrovica and Forte, 1997; Kaufman and Lambeck, 2002; Stuhne and Peltier, 2015; Van der Wal et al., 2015; Peltier et al., 2018; Whitehouse, 2018\). Most of GIA studies address the post Last Glacial Maximum \(LGM\) around 21000 years Before Present \(BP\) deglaciation as a trigger to increasing uplift rates in glaciated regions \(e.g., Peltier, 2004; Whitehouse, 2018\).](#) The magnitude of uplift rates is set primarily by the lithosphere and asthenosphere viscosities, which depend, amongst other factors, on the thermal field at depth (McKenzie and Richter, 1981; McKenzie and Bickle, 1988; Gurnis, 1989; Ranalli, 1995, 1997; Kaufman et al., 1997; Watts, 2001; Turcotte and Schubert, 2002). [While the GIA theory is well developed, few studies use thermo-mechanical visco-elasto-plastic \(non-Newtonian Earth layers\) geodynamic models to estimate uplift rates in response to surface load changes to be compared with GNSS data. Here, we use this approach to constrain the role of the solid Earth rheology in setting the rates of surface vertical displacement in Southern Patagonia, which hosts the biggest continental ice-sheets outside Antarctica and presents ongoing very high rock uplift rates \(Ivins and James, 2004; Dietrich et al., 2010; Lange et al., 2014; Richter et al., 2016; Lenzano et al., 2023\).](#)

The Southern Patagonian Andes in the South American Continent are located above a transition zone between the subducting Antarctic and Nazca plates and a wide asthenospheric window, [where hot buoyant asthenospheric mantle upwells](#) (Fig. 1a; Cande and Leslie, 1986; Breitsprecher and Thorkelson, 2009; Russo et al., 2010, 2022; Dávila et al., 2018; Ávila and

66 [Dávila, 2018, 2020; Mark et al., 2022; Ben-Mansour et al., 2022](#)). The Chile Triple Junction  
67 (CTJ) at  $\sim 46^\circ\text{S}$  delimits the surface tip of the asthenospheric window, which opened during  
68 the last  $\sim 16$  Ma from south to north (Ramos and Kay, 1992; Breitsprecher and Thorkelson,  
69 2009). First order effects of the asthenospheric flow on the surface continental geology are  
70 the inhibition of arc volcanism in favour of retroarc magmatism, [reduction of shortening to](#)  
71 [null or very minor](#), and rock uplift [and exhumation](#) (Ramos and Kay, 1992; Ramos, 2005;  
72 [Lagabrielle et al., 2004, 2010; Breitsprecher and Thorkelson, 2009; Guillaume et al., 2009,](#)  
73 [2013; Scalabrino et al., 2010; Lange et al., 2014; Georgieva et al., 2016, 2019; Ávila and](#)  
74 [Dávila, 2020; Mark et al., 2022; Ávila et al., 2023; Muller et al., 2023](#)). Rock uplift due to  
75 asthenospheric upwelling [occurs through dynamic and thermal effects](#) (Guillaume et al.,  
76 [2009, 2013; Conrad and Husson, 2009; Flament et al., 2013; Sternai et al., 2016b; Dávila et](#)  
77 [al., 2018; Ávila and Dávila, 2020; Faccenna and Becker, 2020; Mark et al., 2022](#)). Dynamic  
78 uplift [occurs above zones of viscous convection of the asthenospheric mantle, generating](#)  
79 [long wavelength \( \$>300\$  km\) deformation of the lithosphere through vertical stresses](#) (Hager  
80 and O'Connell, 1981; Flament et al., 2013, 2015; Sternai et al., 2016b; Ávila and Dávila,  
81 2020; Faccenna and Becker, 2020). This effect [is difficult to measure because vertical](#)  
82 [stresses in the lithosphere occur also due to lithospheric tectonics and the surface mass](#)  
83 [redistribution of glaciers, lakes, and sediments](#) (Lachenbruch and Morgan, 1990; Molnar and  
84 [England, 1990; Watts, 2001](#)). Dynamic uplift was estimated [between 0.02 and 0.15 mm/yr](#) in  
85 the last 3 Ma over an area of about  $100000\text{ km}^2$  around the CTJ latitude (Guillaume et al.,  
86 [2009, 2013; Flament et al., 2015; Ávila and Dávila, 2020; Ávila et al., 2023](#)). The thermal  
87 component is expressed by an increase of temperatures and [shallowing of the lithosphere-](#)  
88 [asthenosphere boundary where asthenospheric mantle upwells](#) (Ávila and Dávila, 2018;  
89 [2020; Russo et al., 2010, 2022; Mark et al., 2022; Ben-Mansour et al., 2022](#)), decreasing the  
90 [integrated elastic lithospheric thickness and generating uplift and higher surface heat flow](#)  
91 [than in normal subduction zones](#) (Ranalli, 1997; Flament et al., 2015; Ávila and Dávila, 2018,  
92 [2020; Ávila et al., 2023](#)). The heat flow was calculated as  $>100\text{ mW/m}^2$  near the CTJ,  $\sim 70\text{-}90$   
93  $\text{mW/m}^2$  in the [centre](#) of the asthenospheric window ( $\sim 50^\circ\text{S}$ ), and  $50\text{-}60\text{ mW/m}^2$  near its  
94 northern boundary ( $\sim 46^\circ\text{S}$ ) (Ávila and Dávila, 2018). [Uplift due to lithospheric thinning was](#)  
95 [estimated as  \$\sim 0.3\$  mm/yr since the middle Miocene in the Southern Patagonian Andes](#) (Pedoja  
96 [et al., 2011; Ávila and Dávila, 2020; Ávila et al., 2023; Ding et al., 2023](#)).

97 The Patagonian Ice Sheet covered the Southern Patagonian Andes between  $\sim 47000$   
98 and  $\sim 17000$  years BP, extending from latitudes  $38^\circ$  to  $55^\circ\text{S}$  with [an](#) estimated area of  
99  $\sim 490000\text{ km}^2$  (Fig. 1 a), [volume of  \$\sim 550000\text{ km}^3\$ , and average and maximum thickness of](#)

1100 and 2500 m, respectively, based on preserved glacial geomorphology, stratigraphy, paleoecology, and geochronological data (Moreno et al., 1999, 2005, 2015; McCulloch et al., 2000, 2005; Hulton et al., 2002; Rabassa, 2008; Glasser et al., 2004, 2005, 2008, 2016; Glasser and Jansson, 2008; Hein et al., 2010; Boex et al., 2013; Strelin et al., 2014; Bourgois et al., 2016; Martinod et al., 2016; Kaplan et al., 2016; Bendle et al., 2017; Thorndycraft et al., 2019; Reynhout et al., 2019; Davies et al., 2020; Yan et al., 2022). ~~Currently, the SPI covers an area of 13219 km<sup>2</sup> with a volume of 3632 ± 675 km<sup>3</sup>, whereas the Northern Patagonian Icefield (NPI) covers an area of 3976 km<sup>2</sup> with a volume of 1124 ± 260 km<sup>3</sup> (Fig. 1). The present-day ice thickness reaches up to 2000 m in deep glacial valleys (Millan et al., 2019).~~ The LGM in Southern Patagonia is estimated around 26000 years BP, but the beginning of significant glacial retreat occurred between 21000 and 17000 years BP (Hulton et al., 2002; Hein et al., 2010; Glasser et al., 2011; Glasser and Davies, 2012; Moreno et al., 2015; Bendle et al., 2017; Reynhout et al., 2019; Davies et al., 2020). Long term ice loss rate is uncertain, but more than 75% of ice was certainly lost since the LGM, and some models predicted more than 95% of ice loss with separation between the Southern Patagonian icefield (SPI) and the Northern Patagonian icefield (NPI) in the first 5000 to 10000 years of post-LGM deglaciation (McCulloch et al., 2000; Hulton et al., 2002; Boex et al., 2013; Bourgois et al., 2016; Thorndycraft et al., 2019; Davies et al., 2020). A glacial minimum must have been attained around 13000 years BP, but several glacial advances were recorded since that time, and the last one was the Little Ice Age (LIA) with apex around 1630 AD, well dated by terminal moraines around the present-day NPI and SPI (Ivins and James, 1999, 2004; McCulloch et al., 2000; Glasser et al., 2004, 2008, 2011; Davies and Glasser, 2012; Strelin et al., 2014; Kaplan et al., 2016; Reynhout et al., 2019; Davies et al., 2020). Recent mass balance measurements in the Patagonian icefields - e.g., Shuttle-Radar Topography Mission (SRTM) or Gravity Recovery and Climate Experiment (GRACE) - often present discrepancies, but consistently show an increasing ice loss from ~15 Gt/yr between ~1940-2000, to ~25 Gt/yr between ~2000-2012 (Aniya, 1996; Aniya et al., 1997; Rignot et al., 2003; Chen et al., 2007; Ivins et al., 2011; Jacob et al., 2012; Willis et al., 2012; Gómez et al., 2022). Currently, the SPI covers an area of ~13219 km<sup>2</sup> with a volume of 3632 ± 675 km<sup>3</sup>, whereas the NPI covers an area of ~3976 km<sup>2</sup> with a volume of 1124 ± 260 km<sup>3</sup> (Fig. 1). The present-day ice thickness may reach up to ~2000 m in deep glacial valleys (Millan et al., 2019).

132 GNSS-measured data show ongoing vertical rock uplift rates between  $18 \pm 3$  and  $41 \pm 3$   
133 mm/yr in the northern part ( $18^\circ - 50.5^\circ \text{ S}$ ) of the SPI (Fig. 1b), decreasing to values between  
134  $2 \pm 6$  and  $17 \pm 5$  mm/yr in its southern part ( $50.5 - 51.5^\circ \text{ S}$ ) (Ivins and James, 2004; Dietrich  
135 et al., 2010; Lange et al., 2014; Richter et al., 2016; Lenzano et al., 2023). Such outstandingly  
136 high uplift rates, specially in the northern part of the SPI, are currently ascribed to  
137 lithospheric viscoelastic GIA following the LIA, which was responsible for an ice loss of  $503$   
138  $\pm 101.1 \text{ km}^3$  in the SPI (Glasser et al., 2011). To match the very high observed uplift rate  
139 budget, previous GIA studies infer low asthenosphere viscosity (in the order of  $10^{18} \text{ Pa s}$ ) and  
140 thin elastic lithosphere ( $\sim 35 \text{ km}$  thick) (Ivins and James, 1999, 2004; Klemann et al., 2007;  
141 Dietrich et al., 2010; Lange et al., 2014; Richter et al., 2016; Ávila and Dávila, 2020; Mark et  
142 al., 2022; Lenzano et al., 2023). Although this is consistent with abnormally high  
143 asthenospheric mantle temperatures, viscosity estimates from these previous studies are  
144 untied to the regional thermal regime, which prevents a more thorough characterization of the  
145 role of the asthenospheric window underneath the SPI in affecting the observed uplift rates.  
146 In addition, the contribution of post-LGM deglaciation to present-day rock uplift rate was  
147 marginally addressed (Ivins and James, 1999, 2004; Klemann et al., 2007). Here, we perform  
148 fully coupled thermo-mechanical numerical geodynamic experiments forced by surface  
149 unloading scaled on post-LIA and post-LGM ice melting to evaluate their relative  
150 contribution to the observed regional uplift rates. Numerical experiments account for a range  
151 of positive thermal anomalies in the asthenosphere to further assess the role of the  
152 asthenospheric window in setting the mantle viscosity and associated postglacial rebound.  
153 Focusing on the magnitude rather than the pattern of the inferred surface uplift rates due to  
154 limited information on the spatial-temporal variations of the ice net mass balance and  
155 thickness since the LGM (e.g. Davies et al., 2020), we use the observed budget of rock uplift  
156 rate to constrain plausible thermal and viscosity structures at depth as well as the timing of  
157 postglacial rebound.

## 159 2. Methodology

160 We used as reference the GNSS-derived data from 31 GPS stations installed by 380  
161 km in north-south and 130 km in east-west directions around the SPI since 1996, published in  
162 Lange et al. (2014). The observed and estimated regional aseismic viscoelastic uplift rates  
163 presented in that study are shown in Fig. 1b. Details on the GPS data acquisition and analysis  
164 are given in the reference study (Lange et al., 2014).

## 2.1. Numerical model

We use a fully coupled thermo-mechanical, visco-elasto-plastic, numerical geodynamic model to quantify the effect of thermal anomalies in the [asthenospheric](#) mantle on the magnitude of surface uplift rates due to deglaciation. We provide a short overview of the governing equations hereafter, while a detailed description of numerical technique can be found, for instance, in Gerya and Yuen (2007), Gerya et al. (2019), [Sternai \(2020\)](#), [Sternai et al. \(2021\)](#), and Muller et al. (2022). The continuity equation allows for the conservation of mass during the displacement of a geological continuum:

$$(1) \quad \frac{\partial \rho}{\partial t} + \nabla(\rho v) = 0$$

where  $\rho$  is the local density,  $t$  is time,  $v$  is the velocity vector, and  $\nabla$  is the divergence operator. The momentum equation describes the changes in velocity of an object in the gravity field due to internal and external forces:

$$(2) \quad \frac{\partial \sigma_{ij}}{\partial x_i} + \rho g_i = \rho \left( \frac{\partial v_i}{\partial t} + v_j \frac{\partial v_i}{\partial x_j} \right)$$

where  $\sigma_{ij}$  is the stress tensor,  $x_i$  and  $x_j$  are spatial coordinates, and  $g_i$  is the  $i$ -th component of the gravity vector. The energy equation allows for the conservation of energy during advective and conductive heat transfer in the continuum:

$$(3) \quad \rho C_p \frac{DT}{Dt} - \text{div}(c \nabla T) + v \nabla T = H_r + H_s + H_a + H_l$$

where  $P$  is pressure,  $T$  is temperature,  $C_p$  is specific heat capacity at a constant  $P$ ,  $c$  is the thermal conductivity,  $H_r + H_s + H_a + H_l$  are the volumetric heat productions by radiogenic, shear, adiabatic and latent heat, respectively.  $H_a \propto \frac{DP}{Dt}$ ,  $H_s = \sigma'_{ij} \dot{\epsilon}'_{ij(\text{viscous})}$ , and  $H_r$  and  $H_l$  are the radiogenic and latent heat productions.

Ductile deformation is thermally activated generating viscous flow, which involves diffusion and dislocation creep, calculated according to the material shear viscosity:

$$(4) \quad \frac{1}{\eta_{\text{ductile}}} = \frac{1}{\eta_{\text{diff}}} + \frac{1}{\eta_{\text{disl}}}$$

with

$$\eta_{\text{diff}} = \frac{\eta_0}{2\sigma_{cr}^{n-1}} \exp\left(\frac{E_a + PV_a}{RT}\right), \text{ and}$$

$$\eta_{\text{disl}} = \frac{\eta_0^{1/n}}{2} \exp\left(\frac{E_a + PV_a}{nRT}\right) \dot{\epsilon}_{II}^{n-1}$$

where  $\eta_{\text{diff}}$  and  $\eta_{\text{disl}}$  are the shear viscosity for diffusion and dislocation creep, respectively,  $\eta_0$  is the material static viscosity,  $\sigma_{cr}$  is the diffusion-dislocation transition critical stress,  $n$  is the stress exponent,  $E_a$  is the activation energy,  $V_a$  is the activation volume,  $R$  is the gas



195 constant, and  $\varepsilon_{II}$  is the second invariant of the strain rate tensor. The viscous deviatoric strain  
 196 rate tensor,  $\dot{\varepsilon}'_{ij(viscous)}$ , is defined by:

$$197 \quad (5) \quad \dot{\varepsilon}'_{ij(viscous)} = \frac{1}{2\eta_{ductile}} \sigma'_{ij} + \delta_{ij} \eta_{bulk} \dot{\varepsilon}_{kk} = \frac{1}{2\eta_{diff}} \sigma'_{ij} + \frac{1}{2\eta_{disl}} \sigma'_{ij} + \delta_{ij} \eta_{bulk} \dot{\varepsilon}_{kk}$$

198 where  $\sigma'_{ij}$  is the deviatoric stress tensor,  $\delta_{ij}$  is the Kronecker delta,  $\dot{\varepsilon}_{kk}$  is the volumetric  
 199 strain rate (e.g., related to phase transformations), and  $\eta_{bulk}$  is the bulk viscosity.  
 200 Recoverable deformation is defined by the elastic deviatoric strain rate tensor,  $\dot{\varepsilon}'_{ij(elastic)}$ , as:

$$201 \quad (6) \quad \dot{\varepsilon}'_{ij(elastic)} = \frac{1}{2\mu} \frac{D\sigma'_{ij}}{Dt}$$

202 where  $\mu$  is the shear modulus and  $\frac{D\sigma'_{ij}}{Dt}$  is the objective co-rotational time derivative of the  
 203 deviatoric stress tensor. The plastic deformation, brittle and localised, occurs at low  
 204 temperature when the absolute shear stress limit,  $\sigma_{yield}$ , is reached, with

$$205 \quad (7) \quad \sigma_{yield} = C + \sin \sin(\varphi)P$$

206 where  $C$  is cohesion and  $\varphi$  is the effective internal friction angle. The plastic strain rate  
 207 tensor,  $\dot{\varepsilon}'_{ij(plastic)}$ , is defined as:

$$208 \quad (8) \quad \dot{\varepsilon}'_{ij(plastic)} = 0 \text{ for } \sigma_{II} < \sigma_{yield}, \dot{\varepsilon}'_{ij(plastic)} = X \frac{\partial \sigma'_{ij}}{\partial \sigma_{II}} \text{ for } \sigma_{II} \geq \sigma_{yield}$$

209 where  $X$  is the plastic multiplier which satisfies the plastic yielding condition  $\sigma_{II} = \sigma_{yield}$ .  
 210 The bulk strain rate tensor,  $\dot{\varepsilon}'_{ij(bulk)}$ , integrates the viscous, elastic and plastic deformation:

$$211 \quad (9) \quad \dot{\varepsilon}'_{ij(bulk)} = \dot{\varepsilon}'_{ij(viscous)} + \dot{\varepsilon}'_{ij(elastic)} + \dot{\varepsilon}'_{ij(plastic)}$$

212

## 213 **2.2. Reference model setup and modeling approach**

214 The model domain is 700 km wide and 120 km thick, [to account for a region similar](#)  
 215 [to the South American continent at latitudes of the SPI, realistic thickness of the lithosphere](#)  
 216 [and asthenospheric mantle \(van der Meijde et al., 2013; Ávila and Dávila, 2018, 2020\), and](#)  
 217 [avoid boundary effects in the numerical results](#). From top to bottom, the model accounts for  
 218 10 km of ‘sticky’ air, 30 km of continental crust (with rheology of quartzite, Ranalli, 1995),  
 219 30 km of lithospheric mantle, and 50 km of asthenospheric mantle (with rheology of dry  
 220 dunite, Ranalli, 1995), in agreement with literature data (e.g., [van der Meijde et al., 2013;](#)  
 221 [Ávila and Dávila, 2018, 2020](#)). The initial geotherm is piece-wise linear resulting from an  
 222 adiabatic temperature gradient of 0.5 °C/km in the asthenosphere (Turcotte and Schubert,  
 223 2002) and thermal boundary conditions equal to 0 °C at the surface and 1327 °C at the  
 224 bottom of the lithosphere, with nil horizontal heat flux across the vertical boundaries. The

225 rheologic and thermal structure of the reference model give a lithospheric elastic thickness,  
226  $T_e$  (*sensu* Burov and Diament, 1995), of ~30 km, comparable to previous estimates  
227 underneath the SPI based on GIA models (Ivins and James, 1999; Dietrich et al., 2010; Lange  
228 et al., 2014), heat flow data (Ávila and Dávila, 2018), waveform inversion (Robertson  
229 Maurice et al., 2003), [and low-temperature thermochronology data \(Thomson et al., 2010;](#)  
230 [Guillaume et al., 2013; Georgieva et al., 2016, 2019; Stevens Goddard and Fosdick, 2019;](#)  
231 [Ávila et al., 2023; Muller et al., 2023\)](#). Rocks rheological properties are listed in Table 1.

232 The numerical model uses the finite differences with marker-in-cell technique,  
233 resolved by  $51 \times 61$  nodes in [the horizontal,  \$x\$ , and vertical,  \$y\$ , directions](#), respectively,  
234 distributed on a Eulerian grid that accounts for a maximum resolution of 1 km along the  $y$   
235 direction in the upper part of the model domain, and ~13 km in the  $x$  direction.  $400 \times 400$   
236 Lagrangian markers are randomly distributed along the  $x$  and  $y$  dimensions and used for  
237 advecting the material properties (Gerya and Yuen, 2007; Gerya et al., 2019). The material  
238 properties carried by Lagrangian markers are then interpolated onto the Eulerian grid via a 4<sup>th</sup>  
239 order Runge-Kutta interpolation scheme. An internal free surface is simulated through the 10  
240 km thick layer of sticky air. The velocity boundary conditions are free slip at all boundaries  
241 ( $x = 0$  and  $x = 700$  km;  $y = 0$  and  $y = 120$  km).

242 On the top of the crust and in the middle of the model domain we impose a 2 km thick  
243 pseudo-icecap to simulate lithospheric unloading during deglaciation ([Fig. 2a](#)). [The pseudo-](#)  
244 [icecap has an initial density,  \$\rho\_{ice}\$ , of  \$920 \text{ kg/m}^3\$  \(Harvey et al., 2017\) \(Table 1\), and we](#)  
245 compute the surface load [through time,  \$L\$](#) , as

$$(10) \quad L = \rho_{ice} g h_{ice},$$

247 where  $g$  is the gravity acceleration, and  $h_{ice}$  is the icecap thickness. [The load change due to](#)  
248 [the deglaciation occurs by gradually and uniformly reducing  \$h\_{ice}\$  in time \(Fig. 2 b, c\)](#). We run  
249 two sets of experiments for the post-LGM deglaciation. In *Model set 1*, 75% of ice loss  
250 occurs in 20000 years (i.e., 1500 m drop of ice thickness, Fig. 2 b), thus assuming a  
251 conservative estimate of ice loss since the beginning of the LGM until the present-day,  
252 [simplifying the several glacial retreats and re-advances since the LGM \(e.g., Glasser et al.,](#)  
253 [2004, 2008, 2011; Davies and Glasser, 2012; Strelin et al., 2014; Kaplan et al., 2016;](#)  
254 [Reynhout et al., 2019\)](#). In *Model set 2*, 95% of ice loss occurs in 10000 years (i.e., 1900 m  
255 drop of ice thickness, Fig. 2 b), assuming faster deglaciation rates of the Patagonian Ice Sheet  
256 in the first half of post-LGM deglaciation (McCulloch et al., 2000; Hulton et al., 2002; Boex  
257 et al., 2013; Bendle et al., 2017; Thorndycraft et al., 2019; Davies et al., 2020). For the post-



258 LIA deglaciation, we simulate 10% of ice loss in 400 years (i.e., 200 m drop of ice thickness,  
259 Fig. 2 c), [using estimates of ice loss rates since the 19<sup>th</sup> century](#) (Aniya, 1996; Aniya et al.,  
260 1997; Rignot et al., 2003; Ivins and James, 1999, 2004; [Chen et al., 2007](#), Dietrich et al.,  
261 2010; [Ivins et al., 2011](#); [Jacob et al., 2012](#); Willis et al., 2012). [The pseudo-icecap is 200 km](#)  
262 [wide for the post-LGM model sets 1 and 2, based on estimates of LGM maximum extent of](#)  
263 [the Patagonian Ice Sheet \(e.g., McCulloch et al., 2000; Hein et al., 2010; Thorndycraft et al.,](#)  
264 [2018; Davies et al., 2020\), and 70 km wide for the post-LIA model set, based on the](#)  
265 [estimates of LIA maximum extent of the SPI \(e.g., Glasser et al., 2011; Strelin et al., 2014;](#)  
266 [Kaplan et al., 2016; Reynhout et al., 2019\) \(Fig. 2 a\).](#)

267 In the models, the lateral extent of the pseudo-icecap does not change throughout the  
268 deglaciation. Although this simplification may affect the inferred pattern of postglacial  
269 rebound, it greatly facilitates the simulation of deglacial lithospheric unloading without  
270 significantly affecting the magnitude of postglacial rebound, which is the main focus here.  
271 All simulations account for some spin up time before the deglaciation begins, so that the  
272 lithosphere-asthenosphere system adjusts to the pseudo-icecap initial load. The uplift rate  
273 during the deglaciation is calculated through time as the surface elevation change resulting  
274 from the modelled strain field divided by the viscoelastic timestep (i.e.,  $U = (z_{curr} -$   
275  $z_{prev})/t$ , where  $z_{curr}$  is the modelled topography at the considered timestep,  $z_{prev}$  is the  
276 modelled topography at the previous timestep, and  $t$  is the viscoelastic timestep duration).  
277 Given the geologically short time window investigated here, we neglect deformation related  
278 to longer term tectonic forces ([Breitsprecher and Thorkelson, 2009](#); [Guillaume et al., 2013](#);  
279 [Eagles and Scott, 2014](#); [Muller et al., 2021](#)). The parametric study focuses on the  
280 [asthenospheric](#) mantle potential temperature (*sensu* McKenzie and Bickle, 1988) which  
281 accounts for positive thermal anomalies, TA, of up to 200 °C in steps of 50 °C, added to the  
282 reference [asthenospheric](#) mantle potential temperature of 1265 °C (McKenzie and Bickle,  
283 1988; Currie and Hyndman, 2006; Ávila and Dávila, 2018, 2020; Sternai, 2020; [Mark et al.,](#)  
284 [2022](#)) to mimic the presence of a slab window at depth.

### 285 | 3. Results

286 | Results are shown in Table 2 and Figs. 4-7. In agreement with the theory of  
287 | lithospheric flexure (e.g., Turcotte and Schubert, 2002) the deglaciation triggers uplift in the  
288 | region covered by the melting pseudo-icecap and subsidence in the neighbouring regions  
289 | (Figs. 4-6). Overall, increasing the [asthenospheric](#) mantle potential temperature decreases the  
290 | asthenospheric viscosity, with significant effects on the magnitude of the modelled surface  
291 | velocity field. The asthenosphere viscosity ranges between  $10^{22}$ - $10^{19}$  Pa s in simulations with  
292 | TA equal to 0 (reference model), 50 and 100 °C, and between  $10^{19}$ - $10^{16}$  Pa s in simulations  
293 | with TA equal to 150 and 200 °C (Fig. 3 a-d). Lithospheric warming due to increasing  
294 | [asthenospheric](#) mantle potential temperature also leads to a reduction of the lower lithosphere  
295 | viscosity (from  $10^{22}$  to  $10^{20}$  Pa s), thereby decreasing the integrated lithospheric strength.

296 | In *Model set 1* for Post-LGM deglaciation, when TA is 0 (reference model) the  
297 | maximum uplift rates is < 1 mm/yr during the first 5000 years of the deglaciation, increasing  
298 | gradually up to 9.5 mm/yr in the later stages of the deglaciation (i.e., 20000 years, Fig. 4).  
299 | When TA equals 50, 100, 150 and 200 °C, the maximum uplift rates can reach up to ~2, ~5,  
300 | ~12, and ~15 mm/yr, respectively, already in the first 1000 years of the deglaciation (Fig. 4  
301 | a). When TA is 50 and 100 °C the maximum uplift rate is subject to a protracted increase in  
302 | time, reaching up to ~12 and ~14 mm/yr after 20000 years of deglaciation (Figs. 4 b-d and 7  
303 | a). For TA equal to 150 and 200 °C, the maximum uplift rate [reaches](#) a plateau between 11  
304 | and 17 mm/yr during the 20000 years of deglaciation (Figs. 4 and 7 a, Table 2a). After the  
305 | end of the deglaciation, the maximum uplift rate takes longer than about 5000 years to re-  
306 | equilibrate to 0 mm/yr when  $TA \leq 100$  °C, whereas it drops to 0 mm/yr almost immediately  
307 | when TA is 150 or 200 °C (Fig. 7 a).

308 | In the *Model set 2* for Post-LGM deglaciation, the maximum uplift rate is less than 2  
309 | mm/yr during the first 1000 years of deglaciation when TA is 0, 50 and 100 °C, whereas it  
310 | reaches up to ~22 and ~30 mm/yr during in the first 1000 years of deglaciation when TA is  
311 | 150 and 200 °C (Fig. 5 a, 7 b, and Table 2). Between 5000 and 10000 years of deglaciation,  
312 | the maximum uplift rate increases to ~19, ~25 and ~36 mm/yr, respectively when TA is 0, 50  
313 | and 100 °C, whereas it reach up to between 36 and 41 mm/yr between 50000 and 1000 years  
314 | of deglaciation when TA equal to 150 and 200 °C. The maximum uplift rate decreases slower  
315 | if TA is 0, 50 and 100 °C, taking longer than 5000 year after the deglaciation to drop to  
316 | values <5 mm/yr (Fig. 7 b and Table 2b), whereas it quickly drops to < 2 mm/yr when the  
317 | deglaciation is over and TA is 150 and 200°C (Figs. 5 b-d and 7b). Overall, a warmer and

318 less viscous asthenosphere generates a higher magnitude and fast changing postglacial  
319 rebound than a cooler and more viscous asthenosphere.

320 In the post-LIA model set, the maximum uplift rate is  $\sim 1.4$ ,  $\sim 2.3$  and  $\sim 2.2$  mm/yr  
321 during the first 100 years of deglaciation when TA is respectively 0, 50, and 100 °C, whereas  
322 it reaches  $\sim 8.3$  and  $\sim 23$  mm/yr during the same interval when TA is respectively 150 and 200  
323 °C (Figs. 6 a, 7 c, and Table 2c). Between 200 and 400 years of deglaciation, the maximum  
324 uplift rate reaches  $\sim 1.9$ ,  $\sim 2.5$  and  $\sim 3$  mm/yr when TA equal to 0, 50 and 100 °C, and  $\sim 14$  and  
325  $\sim 25.5$  mm/yr when TA is 150 and 200 °C, respectively (Figs. 6 c-d, 7 c, and Table 2c). When  
326 the deglaciation ends, the maximum uplift rate drops to  $\sim 0$  mm/yr in  $\sim 100$  years when TA  $\leq$   
327 100 °C, whereas it takes longer than 1000 years when TA equals 150 °C or 200 °C (Fig. 7 c).  
328 Overall, a warmer and less viscous asthenosphere generates a higher magnitude postglacial  
329 rebound which, however, takes much longer to re-equilibrate to 0 mm/yr after the end of the  
330 deglaciation than a cooler and more viscous asthenosphere.

331

#### 332 **4. Discussion**

333 Our modelling is simplistic in that we impose a linear and uniform ice loss instead of  
334 a more realistic ice-sheet melting pattern in space and time (Fig. 2b,c). Although the  
335 stratigraphic and geochronologic record is fairly precise for the post-LGM ice extent (e.g.,  
336 Lagabrielle et al., 2004; Rabassa, 2008; Glasser et al., 2011; Davis and Glasser, 2012; Strelin  
337 et al., 2014; Kaplan et al., 2016; Martinod et al., 2016; Bendle et al., 2017; Reynhout et al.,  
338 2019; Davies et al., 2020), information about melting velocities and associated ice thickness  
339 and redistribution of the surface masses are limited for the time windows investigated here.  
340 GNSS, SRTM, and GRACE data constraining the net ice mass balance only during the last  
341 few decades, still showing some discrepancies (e.g., Aniya, 1996; Aniya et al., 1997; Rignot  
342 et al., 2003; Ivins and James, 1999, 2004; Chen et al., 2007; Dietrich et al., 2010; Ivins et al.,  
343 2011; Jacob et al., 2012; Lange et al., 2014; Willis et al., 2012; Richter et al., 2016; Gómez et  
344 al., 2022; Lenzano et al., 2023). Tracing back the post-LGM or Holocene ice loss rate from  
345 current measurement is difficult, considering that climate was at least 6 °C colder during the  
346 LGM (Hulton et al., 2002; Sugden et al., 2002; Seltzer et al., 2021; Yan et al., 2022). As a  
347 result, previous models have assumed simple deglaciation histories as well (e.g., Ivins and  
348 James, 1999, 2004; Hulton et al., 2002; Klemann, 2007; Ivins et al., 2011; Boex et al, 2013).  
349 Measurements of regional erosion rates since the LGM and the LIA are between 0.02 to 0.83  
350 mm/yr (Fernandez et al., 2016). However, given the short time intervals investigated here, it

351 [seems reasonable to assume that the eroded material is still in the transport zone and therefore](#)  
352 [does not significantly contribute to unloading the surface of the orogen. If one refers to](#)  
353 [erosion rates from low-temperature thermochronology, although these measures quantify](#)  
354 [erosion rates over Myrs and not millennia, Fosdick et al. \(2013\), Herman and Brandon, 2015,](#)  
355 [Fernandez et al., \(2016\), and Muller et al. \(2023\), suggests values between 0.1 and 1 mm/yr](#)  
356 [from 7 to 4 Ma, followed by a period of erosional quiescence \(<0.1 mm/yr\), and a possible](#)  
357 [increase to 1 mm/yr in the last ~2 Ma in the SPI region \(Muller et al., 2023\). Supposing that](#)  
358 [these erosion rates still apply in the last ~20000 years, this would translate into 2-20 m of](#)  
359 [rocks eroded on average since the LGM, leading to local unloading of approximately 60-600](#)  
360 [kPa if one assumes a crustal density of 3000 kg/m<sup>3</sup>. Such stress change is approximately](#)  
361 [equivalent to the melting of about 6-60 m of ice, whereas we simulate the melting of 200-](#)  
362 [1500 m of ice in our simulations. The forcing of Quaternary cooling on increasing erosion](#)  
363 [rates is, however, debated, and not widely quantified in Patagonia nor worldwide \(Valla et](#)  
364 [al., 2012; Champagnac et al., 2014; Herman et al., 2013, 2018; Herman and Brandon, 2015;](#)  
365 [Georgieva et al., 2019; Yan et al., 2022\). Even if long term erosion rates contribute to](#)  
366 [present-day uplift rate \(Herman et al., 2018\), since they are comparable to those of e.g., the](#)  
367 [European Alps, we assume a similar contribution to regional uplift rates \(i.e., generally a](#)  
368 [fraction of a mm/yr; Sternai et al., 2019\), that is a negligible contribution in the context of the](#)  
369 [Southern Patagonian Andes. We also assume a homogeneous lithosphere and neglect lateral](#)  
370 [viscosity variations in the asthenosphere, despite the long-term southern Andean orogenic](#)  
371 [history \(Cande and Leslie, 1986; Ramos, 2005; Breitsprecher and Thorkelson, 2009; Muller](#)  
372 [et al., 2021\) and suggested contribution from lateral rheological heterogeneities \(Klemann et](#)  
373 [al., 2007; Richter et al., 2016\). Overall, notwithstanding these limitations in the model, our](#)  
374 [fully coupled numerical thermo-mechanical geodynamic experiments provide realistic uplift](#)  
375 [rates \(Figs. 4-7\) that one can compare to current geodetic observations. Following the](#)  
376 [example of previous studies \(Ivins and James, 1999, 2004; Klemann et al., 2007; Dietrich et](#)  
377 [al., 2010; Lange et al., 2014; Richter et al., 2016; Lenzano et al., 2023\), we discuss our results](#)  
378 [assuming that GNSS-measured rock uplift rates are mostly related to the deglaciation history](#)  
379 [and only marginally controlled by the longer term geodynamics \(e.g., Ramos, 2005;](#)  
380 [Breitsprecher and Thorkelson, 2009; Eagles and Scott, 2014; Muller et al., 2021\).](#)

381 [The elastic thickness of the lithosphere \( \$T\_e\$ \) varies between the simulations according](#)  
382 [to the imposed asthenospheric thermal anomaly, but it is generally lower than 30 km,](#)  
383 [resulting in a decoupled lithospheric rheology \(\*sensu\* e.g., Burov and Diament, 1995\), as](#)  
384 [shown by the yield stress envelope in Fig. 2a. This results in predominant elastic deformation](#)

385 [in the upper crust \(below the ~300 °C isotherm\)](#) and upper mantle lithosphere (below the  
386 [~700 °C isotherm\)](#) and viscous [deformation in the lower crust, lower lithospheric mantle and](#)  
387 [asthenosphere \(Fig. 3\)](#). We remark that, when we impose higher temperatures in the  
388 [asthenospheric mantle, shallower 300 °C and 700 °C isotherms decreases  \$T\_e\$  and increases](#)  
389 [the isostatic surface uplift rates. Lithospheric thinning due to the asthenospheric window](#)  
390 [underneath Southern Patagonia thus affects the regional uplift rates as previously suggested](#)  
391 [\(Avila and Davila, 2018, 2020; Mark et al., 2022; Ben-Mansour et al., 2022; and Avila et al.,](#)  
392 [2023\)](#).

393 [The](#) inferred maximum post-LIA uplift rate of up to a few mm/yr from experiments  
394 without or with a low asthenospheric thermal anomaly ( $TA \leq 100$  °C, [Fig. 7c](#)) are within the  
395 same order of magnitude of maximum uplift rates measured in collisional orogens such as the  
396 European Alps (Sue et al., 2007; Serpelloni et al., 2013; Walpersdorf et al., 2015; Sternai et  
397 al., 2019) and the Himalayas (Larson et al., 1999). Since these collisional orogens are  
398 [characterised](#) by a thicker lithosphere (Geissler et al., 2010; Ravikumar et al., 2020), they are  
399 likely less sensitive to mantle dynamics than the Southern Patagonian Andes. When we  
400 consider lithospheric unloading due to post-LGM deglaciation of a wider ice sheet, however,  
401 the inferred maximum uplift rate via *Model set 1* and *Model set 2* reaches up to 10 mm/yr for  
402 and 20 mm/yr, respectively, even without asthenospheric thermal anomaly ([Fig. 7a,b](#)). This  
403 suggests a [likely](#) contribution from long-term postglacial rebound to the present-day uplift  
404 rates measured in the SPI.

405 In the Southern Patagonian Andes, [GIA models estimated](#) the regional asthenosphere  
406 viscosity between  $1.6$  and  $8 \times 10^{18}$  Pa s (Ivins and James, 1999, 2004; Dietrich et al., 2010;  
407 Willis et al., 2012; Lange et al., 2014; [Richter et al., 2016; Lenzano et al., 2023](#)). Similarly,  
408 the asthenosphere viscosity from our models when  $TA > 100$  °C is  $< 10^{19}$  Pa s, with the  
409 lowest viscosity value of  $10^{16}$  Pa s imposed where partial melting, supported by the regional  
410 Holocene volcanism (Stern and Kilian, 1996) [and by geophysical data \(e.g., shear wave](#)  
411 [velocity data by Mark et al., 2022\)](#), occurs. Under these conditions, however, our experiments  
412 provide [max](#) uplift rates between 14 and 26 mm/yr [toward the end of the](#) LIA deglaciation  
413 ([Fig. 7c](#)). [Even](#) with a very low viscosity asthenosphere, the rebound due to short-term post-  
414 LIA deglaciation does not reach the presently observed maximum uplift rates of  $41 \pm 3$   
415 mm/yr. Experiments that account for a low viscosity asthenosphere and long-term post-LGM  
416 deglaciation lasting for 20000 years and 10000 years reach up to  $\sim 25$  and  $\sim 42$  mm/yr of uplift  
417 rate [during the final stages of the deglaciation \(Fig. 7a-b\)](#), respectively, comparable to  
418 present-day values. Results, therefore, indicate that the outstanding observational budget of

419 rock uplift in the SPI is matched only when accounting for higher-than-normal  
420 asthenospheric mantle temperatures, thereby highlighting the relevance of the regional  
421 asthenospheric window. Consistently, although the higher heat flow is currently further north  
422 from our study region, near the CTJ (46-48 °S) (Ramos, 2005; Breitsprecher and Thorkelson,  
423 2009; Avila and Davila, 2018, 2020; Ben-Mansour et al., 2022), increased asthenospheric  
424 temperatures beneath the Southern Patagonia is highly supported by the geophysical data  
425 (e.g., Russo et al., 2010, 2022; Mark et al., 2022; Avila and Davila, 2018, 2020; Ben-  
426 Mansour et al., 2022).

427 Because of the limited knowledge regarding the timing and amount of ice loss since  
428 the LGM (e.g., Ivins and James, 1999, 2004; Hulton et al., 2002; Klemann, 2007; Boex et al,  
429 2013; Davies et al., 2020), it is difficult to position in time present-day uplift rate  
430 measurements within the investigated deglaciation scenarios to assess the contribution of  
431 post-LGM, post-LIA, and present-day deglaciation to the maximum uplift rate budget. In the  
432 faster post-LGM deglaciation scenario (*Model set 2*) the observed maximum uplift rate  
433 budget is attained in about 10000 years of deglaciation, but only minor residual rebound  
434 could be observed today regardless of the amount of ice loss (Fig. 7 b). If post-LGM  
435 deglaciation occurred slower (*Model set 1*), this event may contribute up to 40% to the  
436 present-day uplift rate budget (Fig. 7a). Although it is difficult to reconcile this scenario with  
437 the geomorphological and geochronological evidences (Hulton et al., 2002; Boex et al., 2013;  
438 Davis and Glasser, 2012; Martinod et al., 2016; Bendle et al., 2017; Thorndycraft et al., 2019;  
439 Davies et al., 2020), it appears that post-LIA rebound alone cannot cover the entire budget of  
440 the observed uplift rates even with the highest tested TA, which points to a non-negligible  
441 contribution from post-LGM deglaciation. This latter conclusion is reinforced by estimates of  
442 the mantle relaxation time,  $\tau_r$ , as (Turcotte and Schubert, 2002):

$$443 \quad (11) \quad \tau_r = \frac{4\pi\nu}{g\lambda},$$

444 where  $\nu$  is the asthenosphere viscosity,  $\lambda$  is the width of the ice sheet, and  $g$  is the  
445 gravity acceleration. Using  $10^{16} < \nu < 10^{18}$  Pa s and  $\lambda = 200$  km leads to  $\sim 2000 < \tau_r < \sim 200000$   
446 years, a time range considerably longer than the post-LIA deglaciation and including full  
447 Pleistocene glacial-interglacial cycles (Ruddiman et al., 1986). Although increasingly  
448 negative ice mass balance in the last ~50 years contribute to the elastic lithospheric uplift  
449 rates (Dietrich et al., 2010, Lange et al., 2014), a longer term contribution from the viscous  
450 lithosphere is necessary to explain the GNSS-measured uplift rates and (Ivins and James,  
451 2004; Dietrich et al., 2010; Lange et al., 2014; Richter et al., 2016; Lenzano et al., 2021).



452 As a final consideration, our models suggest that we shall measure regional uplift  
453 rates in the order of the tens of cm/yr in the next century if the currently observed ice loss rate  
454 of at least -20 Gt/yr in the SPI (Willis et al., 2012) will continue until the total meltdown of  
455 the ice sheet in ~200 years.

## 456 5. Conclusions

457  
458  
459 We propose that rock uplift rates of up to 40 mm/yr in the Southern Andes are due to  
460 both post-LIA and long-term post-LGM lithospheric rebound, as postulated for other  
461 glaciated orogens (e.g., the European Alps, Fennoscandia, and North America, Peltier et al.,  
462 2018). We also propose that currently observed uplift rates in the Southern Andes are  
463 enhanced by a mantle thermal anomaly of at least 150 °C due to the regional asthenospheric  
464 window. Asthenospheric thermal anomalies higher than 200 °C are unlikely and would  
465 decrease the asthenospheric viscosities to unrealistic values (less than  $10^{16}$  Pa s). Our thermo-  
466 mechanical visco-elasto-plastic forward modelling approach thus helps constraining the  
467 increase in temperature in geodynamic asthenospheric upwelling contexts such as in Southern  
468 Patagonia (Russo et al., 2010, 2022; Avila and Davila, 2018, 2020; Mark et al., 2022; Ben-  
469 Mansour et al., 2022).

470 ~~As a final consideration, our models suggest that we shall measure regional uplift~~  
471 ~~rates in the order of the tens of cm/yr in the next century if the currently observed ice loss rate~~  
472 ~~of at least -20 Gt/yr in the SPI (Willis et al., 2012) will continue until the total meltdown of~~  
473 ~~the ice sheet in 200 years.~~

## 474 475 **5. Acknowledgements**

476  
477 This work was supported by the Italian Ministry of Education, MUR (Project  
478 Dipartimenti di Eccellenza 2023-2027, TECLA, Department of Earth and Environmental  
479 Sciences, University of Milano-Bicocca), and the Fondazione Cariplo and Fondazione CDP  
480 (Grant n° 2022 – 1546\_001). The Université Grenoble Alpes and the French CNRS also  
481 supported this work. We acknowledge the enriching revisions of Federico Dávila, Joelle  
482 Nicolas, and one anonymous referee.

484 **References**

- 485 Aniya, M., Sato, H., Naruse, R., Skvarca, P., [and](#) Casassa, G.: Recent glacier variations in the  
486 Southern Patagonia icefield, South America, *Arctic and Alpine Research*, 29(1), 1-12,  
487 <https://doi.org/10.1080/00040851.1997.12003210>, 1997.
- 488 Aniya, M.: Holocene variations of Ameghino glacier, southern Patagonia, *The Holocene*,  
489 6(2), 247-252, <https://doi.org/10.1177/095968369600600211>, 1996.
- 490 Ávila, P., [and](#) Dávila, F. M.: Heat flow and lithospheric thickness analysis in the Patagonian  
491 asthenospheric windows, southern South America, *Tectonophysics*, 747, 99-107,  
492 <https://doi.org/10.1016/j.tecto.2018.10.006>, 2018.
- 493 [Ávila, P., and Dávila, F. M.: Lithospheric thinning and dynamic uplift effects during slab](#)  
494 [window formation, southern Patagonia \(45-55 S\), \*Journal of Geodynamics\*, 133, 101689,](#)  
495 <https://doi.org/10.1016/j.jog.2019.101689>, 2020.
- 496 [Ávila, P., Ávila, M., Dávila, F. M., Ezpeleta, M., and Castellano, N. E.: Patagonian landscape](#)  
497 [modeling during Miocene to Present-day slab window formation, \*Tectonophysics\*, 229971,](#)  
498 <https://doi.org/10.1016/j.tecto.2023.229971>, 2023.
- 499 [Ben-Mansour, W., Wiens, D. A., Mark, H. F., Russo, R. M., Richter, A., Marderwald, E., and](#)  
500 [Barrientos, S.: Mantle flow pattern associated with the patagonian slab window determined](#)  
501 [from azimuthal anisotropy, \*Geophysical Research Letters\*, 49\(18\), e2022GL099871,](#)  
502 <https://doi.org/10.1029/2022GL099871>, 2022.
- 503 Bendle, J. M., Palmer, A. P., Thorndycraft, V. R., [and](#) Matthews, I. P.: High-resolution  
504 chronology for deglaciation of the Patagonian Ice Sheet at Lago Buenos Aires (46.5 S)  
505 revealed through varve chronology and Bayesian age modelling, *Quaternary Science*  
506 *Reviews*, 177, 314-339, <https://doi.org/10.1016/j.quascirev.2017.10.013>, 2017.
- 507 Boex, J., Fogwill, C., Harrison, S., Glasser, N. F., Hein, A., Schnabel, C., [and](#) Xu, S.: Rapid  
508 thinning of the late Pleistocene Patagonian Ice Sheet followed migration of the Southern  
509 Westerlies, *Scientific Reports*, 3(1), 1-6, <https://doi.org/10.1038/srep02118>, 2013.
- 510 Bourgois, J., Cisternas, M. E., Braucher, R., Bourlès, D., [and](#) Frutos, J.: Geomorphic records  
511 along the general Carrera (Chile)–Buenos Aires (Argentina) glacial lake (46–48 S), climate  
512 inferences, and glacial rebound for the past 7–9 ka, *The Journal of Geology*, 124(1), 27-53,  
513 <https://doi.org/10.1086/684252>, 2016.
- 514 Breitsprecher, K., [and](#) Thorkelson, D. J.: Neogene kinematic history of Nazca–Antarctic–  
515 Phoenix slab windows beneath Patagonia and the Antarctic Peninsula, *Tectonophysics*,  
516 464(1-4), 10-20, <https://doi.org/10.1016/j.tecto.2008.02.013>, 2009.
- 517 Burov, E. B., [and](#) Diament, M.: The effective elastic thickness ( $T_e$ ) of continental  
518 lithosphere: What does it really mean? *Journal of Geophysical Research: Solid Earth*,  
519 100(B3), 3905-3927, <https://doi.org/10.1029/94JB02770>, 1995.
- 520 Butler, S. L., [and](#) Peltier, W. R.: On scaling relations in time-dependent mantle convection  
521 and the heat transfer constraint on layering, *Journal of Geophysical Research: Solid Earth*,  
522 105(B2), 3175-3208, <https://doi.org/10.1029/1999JB900377>, 2000.
- 523 Cande, S. C., [and](#) Leslie, R. B.: Late Cenozoic tectonics of the southern Chile trench, *Journal*  
524 *of Geophysical Research: Solid Earth*, 91(B1), 471-496,  
525 <https://doi.org/10.1029/JB091iB01p00471>, 1986.
- 526 Champagnac, J. D., Molnar, P., Sue, C., [and](#) Herman, F.: Tectonics, climate, and mountain

527 topography, *Journal of Geophysical Research: Solid Earth*, 117(B2),  
528 <https://doi.org/10.1029/2011JB008348>, 2012.

529 [Champagnac, J.-D., Valla, P. G., and Herman, F.: Late-cenozoic relief evolution under](#)  
530 [evolving climate: A review, \*Tectonophysics\*, 614, 44–65,](#)  
531 <https://doi.org/10.1016/j.tecto.2013.11.037>, 2014.

532 [Chen, J. L., Wilson, C. R., Tapley, B. D., Blankenship, D. D., and Ivins, E. R.: Patagonia](#)  
533 [icefield melting observed by gravity recovery and climate experiment \(GRACE\),](#)  
534 [Geophysical Research Letters](#), 34(22), <https://doi.org/10.1029/2007GL031871>, 2007.

535 Cloetingh, S., Sternai, P., Koptev, A., Ehlers, T. A., Gerya, T., Kovács, I., Oerlemans, J.,  
536 Beekman, F., Lavallée, Y., Dingwell, D., Békési, E., Porkoláb, K., Tesauro, M., Lavecchia,  
537 A., Botsyun, S., Muller, V., Roure, F., Serpelloni, E., Matenco, L., Castelltort, S.,  
538 Giovannelli, D., Brovarone, A.V., Malaspina, N., Coletti, G., Valla, P., and Limberger, J.:  
539 Coupled surface to deep Earth processes: Perspectives from TOPO-EUROPE with an  
540 emphasis on climate-and energy-related societal challenges, *Global and Planetary Change*,  
541 104140, <https://doi.org/10.1016/j.gloplacha.2023.104140>, 2023.

542 [Conrad, C. P., and Husson, L.: Influence of dynamic topography on sea level and its rate of](#)  
543 [change, \*Lithosphere\*, 1\(2\), 110-120, https://doi.org/10.1130/L32.1, 2009.](#)

544 Currie, C. A., and Hyndman, R. D.: The thermal structure of subduction zone back arcs,  
545 *Journal of Geophysical Research: Solid Earth*, 111(B8),  
546 <https://doi.org/10.1029/2005JB004024>, 2006.

547 Davies, B. J., and Glasser, N. F.: Accelerating shrinkage of Patagonian glaciers from the  
548 Little Ice Age (~ AD 1870) to 2011, *Journal of Glaciology*, 58(212), 1063-1084,  
549 <https://doi.org/10.3189/2012JoG12J026>, 2012.

550 Davies, B. J., Darvill, C. M., Lovell, H., Bendle, J. M., Dowdeswell, J. A., Fabel, D., García,  
551 J.-L., Geiger, A., Glasser, N.F., Gheorghiu, D.M., Harrison, S., Hein, A.S., Kaplan, M.R.,  
552 Martin, J.R.V., Mendelova, M., Palmer, A., Pelto, M., Rodés, A., Segredo, E.A., Smedley,  
553 R.K., Smellie J., and Thorndycraft, V. R.: The evolution of the Patagonian Ice Sheet from 35  
554 ka to the present day (PATICE), *Earth-Science Reviews*, 204, 103152,  
555 <https://doi.org/10.1016/j.earscirev.2020.103152>, 2020.

556 [Dávila, F. M., Lithgow-Bertelloni, C., Martina, F., Ávila, P., Nóbile, J., Collo, G., Ezpeleta,](#)  
557 [M., Canelo, H., and Sánchez, F.: Mantle influence on Andean and pre-Andean topography,](#)  
558 [in: \*The Evolution of the Chilean-Argentinean Andes\*, edited by Folguera, A. et al., Springer](#)  
559 [Earth System Sciences](#), 363-385, 2018.

560 Dietrich, R., Ivins, E. R., Casassa, G., Lange, H., Wendt, J., and Fritsche, M.: Rapid crustal  
561 uplift in Patagonia due to enhanced ice loss. *Earth and Planetary Science Letters*, 289(1-2),  
562 22-29, <https://doi.org/10.1016/j.epsl.2009.10.021>, 2010.

563 [Ding, X., Dávila, F. M., and Lithgow-Bertelloni, C.: Mechanisms of subsidence and uplift of](#)  
564 [Southern Patagonia and offshore basins during slab window formation, \*Geochemistry,\*](#)  
565 [Geophysics, Geosystems](#), 24(5), e2022GC010844, <https://doi.org/10.1029/2022GC010844>,  
566 2023.

567 [Faccenna, C., and Becker, T. W.: Topographic expressions of mantle dynamics in the](#)  
568 [Mediterranean. \*Earth-Science Reviews\*, 209, 103327,](#)  
569 <https://doi.org/10.1016/j.earscirev.2020.103327>, 2020.

570 [Fernandez, R. A., Anderson, J. B., Wellner, J. S., Totten, R. L., Hallet, B., and Smith, R. T.:](#)  
571 [Latitudinal variation in glacial erosion rates from Patagonia and the Antarctic Peninsula \(46](#)

572 [S–65 S\), GSA Bulletin, 128\(5-6\), 1000-1023, https://doi.org/10.1130/B31321.1, 2016.](https://doi.org/10.1130/B31321.1)

573 [Flament, N., Gurnis, M., and Müller, R. D.: A review of observations and models of dynamic](https://doi.org/10.1130/L245.1)  
574 [topography, Lithosphere, 5\(2\), 189-210, https://doi.org/10.1130/L245.1, 2013.](https://doi.org/10.1130/L245.1)

575 [Flament, N., Gurnis, M., Müller, R. D., Bower, D. J., and Husson, L.: Influence of subduction](https://doi.org/10.1016/j.epsl.2015.08.006)  
576 [history on South American topography, Earth and Planetary Science Letters, 430, 9-18,](https://doi.org/10.1016/j.epsl.2015.08.006)  
577 [https://doi.org/10.1016/j.epsl.2015.08.006, 2015.](https://doi.org/10.1016/j.epsl.2015.08.006)

578 [Fosdick, J. C., Grove, M., Hourigan, J. K., and Calderon, M.: Retroarc deformation and](https://doi.org/10.1016/j.epsl.2012.12.007)  
579 [exhumation near the end of the Andes, southern Patagonia, Earth and Planetary Science](https://doi.org/10.1016/j.epsl.2012.12.007)  
580 [Letters, 361, 504-517, https://doi.org/10.1016/j.epsl.2012.12.007, 2013.](https://doi.org/10.1016/j.epsl.2012.12.007)

581 Geissler, W. H., Sodoudi, F., and Kind, R.: Thickness of the central and eastern European  
582 lithosphere as seen by S receiver functions, Geophysical Journal International, 181(2), 604-  
583 634, [https://doi.org/10.1111/j.1365-246X.2010.04548.x, 2010.](https://doi.org/10.1111/j.1365-246X.2010.04548.x)

584 [Georgieva, V., Gallagher, K., Sobczyk, A., Sobel, E. R., Schildgen, T. F., Ehlers, T. A., and](https://doi.org/10.1016/j.epsl.2019.01.030)  
585 [Strecker, M. R.: Effects of slab-window, alkaline volcanism, and glaciation on](https://doi.org/10.1016/j.epsl.2019.01.030)  
586 [thermochronometer cooling histories, Patagonian Andes, Earth and Planetary Science Letters,](https://doi.org/10.1016/j.epsl.2019.01.030)  
587 [511, 164-176, https://doi.org/10.1016/j.epsl.2019.01.030, 2019.](https://doi.org/10.1016/j.epsl.2019.01.030)

588 Georgieva, V., Melnick, D., Schildgen, T. F., Ehlers, T. A., Lagabrielle, Y., Enkelmann, E.,  
589 and Strecker, M. R.: Tectonic control on rock uplift, exhumation, and topography above an  
590 oceanic ridge collision: Southern Patagonian Andes (47 S), Chile, Tectonics, 35(6), 1317-  
591 1341, [https://doi.org/10.1002/2016TC004120, 2016.](https://doi.org/10.1002/2016TC004120)

592 Gerya, T. (Ed.): Introduction to numerical geodynamic modelling. Cambridge University  
593 Press, ISBN 978-1-107-14314-2, 2019

594 Gerya, T. V., and Yuen, D. A.: Robust characteristics method for modelling multiphase  
595 visco-elasto-plastic thermo-mechanical problems, Physics of the Earth and Planetary  
596 Interiors, 163(1-4), 83-105, [https://doi.org/10.1016/j.pepi.2007.04.015, 2007.](https://doi.org/10.1016/j.pepi.2007.04.015)

597 Glasser, N. F., Harrison, S., Jansson, K. N., Anderson, K., and Cowley, A.: Global sea-level  
598 contribution from the Patagonian Icefields since the Little Ice Age maximum, Nature  
599 Geoscience, 4(5), 303-307, [https://doi.org/10.1038/ngeo1122, 2011.](https://doi.org/10.1038/ngeo1122)

600 [Glasser, N. F., Harrison, S., Winchester, V., and Aniya, M.: Late Pleistocene and Holocene](https://doi.org/10.1016/j.gloplacha.2004.03.002)  
601 [palaeoclimate and glacier fluctuations in Patagonia, Global and planetary change, 43\(1-2\),](https://doi.org/10.1016/j.gloplacha.2004.03.002)  
602 [79-101, https://doi.org/10.1016/j.gloplacha.2004.03.002, 2004.](https://doi.org/10.1016/j.gloplacha.2004.03.002)

603 Glasser, N. F., Jansson, K. N., Duller, G. A., Singarayer, J., Holloway, M., and Harrison, S.:  
604 Glacial lake drainage in Patagonia (13-8 kyr) and response of the adjacent Pacific Ocean,  
605 Scientific reports, 6(1), 21064, [https://doi.org/10.1038/srep21064, 2016.](https://doi.org/10.1038/srep21064)

606 [Glasser, N. F., Jansson, K. N., Harrison, S., and Kleman, J.: The glacial geomorphology and](https://doi.org/10.1016/j.quascirev.2007.11.011)  
607 [Pleistocene history of South America between 38 S and 56 S, Quaternary Science Reviews,](https://doi.org/10.1016/j.quascirev.2007.11.011)  
608 [27\(3-4\), 365-390, https://doi.org/10.1016/j.quascirev.2007.11.011, 2008.](https://doi.org/10.1016/j.quascirev.2007.11.011)

609 Glasser, N. F., Jansson, K. N., Harrison, S., and Rivera, A.: Geomorphological evidence for  
610 variations of the North Patagonian Icefield during the Holocene, Geomorphology, 71(3-4),  
611 263-277, [https://doi.org/10.1016/j.geomorph.2005.02.003, 2005.](https://doi.org/10.1016/j.geomorph.2005.02.003)

612 Glasser, N., and Jansson, K.: The glacial map of southern South America, Journal of Maps,  
613 4(1), 175-196, [https://doi.org/10.4113/jom.2008.1020, 2008.](https://doi.org/10.4113/jom.2008.1020)

614 [Gómez, D. D., Bevis, M. G., Smalley Jr, R., Durand, M., Willis, M. J., Caccamise, D. J.,](https://doi.org/10.1016/j.epsl.2019.01.030)  
615 [Kendrick, E., Skvarca, P., Sobrero, F. S., Parra, H., and Casassa, G.: Transient ice loss in the](https://doi.org/10.1016/j.epsl.2019.01.030)

616 [Patagonia Icefields during the 2015–2016 El Niño event, Scientific Reports, 12\(1\), 9553,](https://doi.org/10.1038/s41598-022-13252-8)  
617 [https://doi.org/10.1038/s41598-022-13252-8, 2022.](https://doi.org/10.1038/s41598-022-13252-8)

618 [Guillaume, B., Gautheron, C., Simon-Labric, T., Martinod, J., Roddaz, M., and Douville, E.:  
619 \[Dynamic topography control on Patagonian relief evolution as inferred from low temperature  
620 \\[thermochronology, Earth and Planetary Science Letters, 364, 157-167,\\]\\(https://doi.org/10.1016/j.epsl.2012.12.036\\)  
621 \\[https://doi.org/10.1016/j.epsl.2012.12.036, 2013.\\]\\(https://doi.org/10.1016/j.epsl.2012.12.036\\)\]\(https://doi.org/10.1016/j.epsl.2012.12.036\)](https://doi.org/10.1016/j.epsl.2012.12.036)

622 Guillaume, B., Martinod, J., Husson, L., Roddaz, M., [and Riquelme, R.:](https://doi.org/10.1029/2008TC002324) Neogene uplift of  
623 central eastern Patagonia: dynamic response to active spreading ridge subduction? *Tectonics*,  
624 28(2), [https://doi.org/10.1029/2008TC002324, 2009.](https://doi.org/10.1029/2008TC002324)

625 Gurnis, M. A.: reassessment of the heat transport by variable viscosity convection with plates  
626 and lids, *Geophysical Research Letters*, 16(2), 179-182,  
627 [https://doi.org/10.1029/GL016i002p00179, 1989.](https://doi.org/10.1029/GL016i002p00179)

628 [Harvey, A. H.: Properties of Ice and Supercooled Water, in: CRC Handbook of Chemistry  
629 \[and Physics \\(97th ed.\\), edited by: Haynes, W. M.; Lide, D. R.; Bruno, T. J., Boca Raton, FL:  
630 \\[CRC Press, ISBN 978-1-4987-5429-3, 2017.\\]\\(https://doi.org/10.1002/9781118133201.ch17\\)\]\(https://doi.org/10.1002/9781118133201.ch17\)](https://doi.org/10.1002/9781118133201.ch17)

631 Hein, A. S., Hulton, N. R., Dunai, T. J., Sugden, D. E., Kaplan, M. R., [and Xu, S.:](https://doi.org/10.1016/j.quascirev.2010.01.020) The  
632 chronology of the Last Glacial Maximum and deglacial events in central Argentine  
633 Patagonia, *Quaternary Science Reviews*, 29(9-10), 1212-1227,  
634 [https://doi.org/10.1016/j.quascirev.2010.01.020, 2010.](https://doi.org/10.1016/j.quascirev.2010.01.020)

635 [Herman, F., and Brandon, M.: Mid-latitude glacial erosion hotspot related to equatorial shifts  
636 \[in southern Westerlies, Geology, 43\\(11\\), 987-990, https://doi.org/10.1130/G37008.1, 2015.\]\(https://doi.org/10.1130/G37008.1\)](https://doi.org/10.1130/G37008.1)

637 [Herman, F., Braun, J., Deal, E., and Prasicsek, G.: The response time of glacial erosion,  
638 \[Journal of Geophysical Research: Earth Surface, 123\\(4\\), 801-817,  
639 \\[https://doi.org/10.1002/2017JF004586, 2018.\\]\\(https://doi.org/10.1002/2017JF004586\\)\]\(https://doi.org/10.1002/2017JF004586\)](https://doi.org/10.1002/2017JF004586)

640 [Herman, F., Seward, D., Valla, P. G., Carter, A., Kohn, B., Willett, S. D., and Ehlers, T. A.:  
641 \[Worldwide acceleration of mountain erosion under a cooling climate, Nature, 504\\(7480\\),  
642 \\[423–426, https://doi.org/10.1038/nature12877, 2013.\\]\\(https://doi.org/10.1038/nature12877\\)\]\(https://doi.org/10.1038/nature12877\)](https://doi.org/10.1038/nature12877)

643 Hirschmann, M. M.: Mantle solidus: Experimental constraints and the effects of peridotite  
644 composition, *Geochemistry, Geophysics, Geosystems*, 1(10),  
645 [https://doi.org/10.1029/2000GC000070, 2000.](https://doi.org/10.1029/2000GC000070)

646 Hulton, N. R., Purves, R. S., McCulloch, R. D., Sugden, D. E., [and Bentley, M. J.:](https://doi.org/10.1016/S0277-3791(01)00103-2) The last  
647 glacial maximum and deglaciation in southern South America, *Quaternary Science Reviews*,  
648 21(1-3), 233-241, [https://doi.org/10.1016/S0277-3791\(01\)00103-2, 2002.](https://doi.org/10.1016/S0277-3791(01)00103-2)

649 Ivins, E. R., [and James, T. S.](https://doi.org/10.1029/2004GL021500) Bedrock response to Llanquihue Holocene and present-day  
650 glaciation in southernmost South America. *Geophysical Research Letters*, 31(24),  
651 [https://doi.org/10.1029/2004GL021500, 2004.](https://doi.org/10.1029/2004GL021500)

652 Ivins, E. R., [and James, T. S.:](https://doi.org/10.1046/j.1365-246x.1999.00899.x) Simple models for late Holocene and present-day Patagonian  
653 glacier fluctuations and predictions of a geodetically detectable isostatic response,  
654 *Geophysical Journal International*, 138(3), 601-624, [https://doi.org/10.1046/j.1365-  
655 \[246x.1999.00899.x, 1999.\]\(https://doi.org/10.1046/j.1365-246x.1999.00899.x\)](https://doi.org/10.1046/j.1365-246x.1999.00899.x)

656 Ivins, E. R., Watkins, M. M., Yuan, D. N., Dietrich, R., Casassa, G., [and Rülke, A.:](https://doi.org/10.1029/2010JB007607) On-land  
657 ice loss and glacial isostatic adjustment at the Drake Passage: 2003–2009, *Journal of  
658 [Geophysical Research: Solid Earth, 116\(B2\), https://doi.org/10.1029/2010JB007607, 2011.](https://doi.org/10.1029/2010JB007607)*

659 [Jacob, T., Wahr, J., Pfeffer, W. T., and Swenson, S.: Recent contributions of glaciers and ice](https://doi.org/10.1002/9781118133201.ch17)



660 caps to sea level rise, *Nature*, 482(7386), 514-518, <https://doi.org/10.1038/nature10847>,  
661 2012.

662 Johannes, W.: The significance of experimental studies for the formation of migmatites, *in*:  
663 *Migmatites*, edited by: Ashworth, J. R., Blackie & Son Ltd, USA Chapman & Hall, 1985.

664 Kaplan, M. R., Schaefer, J. M., Strelin, J. A., Denton, G. H., Anderson, R. F., Vandergoes,  
665 M. J., Finkel, R. C., Schwartz, R., Travis, S. G., Garcia, J. L., Martini, M. A., and Nielsen, S.  
666 H. H.: Patagonian and southern South Atlantic view of Holocene climate, *Quaternary Science*  
667 *Reviews*, 141, 112-125, <https://doi.org/10.1016/j.quascirev.2016.03.014>, 2016.

668 Kaufmann, G., and Lambeck, K.: Glacial isostatic adjustment and the radial viscosity profile  
669 from inverse modelling, *Journal of Geophysical Research: Solid Earth*, 107(B11), ETG-5,  
670 <https://doi.org/10.1029/2001JB000941>, 2002.

671 Kaufmann, G., Wu, P., and Wolf, D.: Some effects of lateral heterogeneities in the upper  
672 mantle on postglacial land uplift close to continental margins, *Geophysical Journal*  
673 *International*, 128(1), 175-187, <https://doi.org/10.1111/j.1365-246X.1997.tb04078.x>, 1997.

674 Klemann, V., Ivins, E. R., Martinec, Z., and Wolf, D.: Models of active glacial isostasy  
675 roofing warm subduction: Case of the South Patagonian Ice Field, *Journal of Geophysical*  
676 *Research: Solid Earth*, 112(B9), <https://doi.org/10.1029/2006JB004818>, 2007.

677 Lachenbruch, A. H., and Morgan, P.: Continental extension, magmatism and elevation;  
678 formal relations and rules of thumb, *Tectonophysics*, 174(1-2), 39-62,  
679 [https://doi.org/10.1016/0040-1951\(90\)90383-J](https://doi.org/10.1016/0040-1951(90)90383-J), 1990.

680 Lagabrielle, Y., Scalabrino, B., Suarez, M., and Ritz, J. F.: Mio-Pliocene glaciations of  
681 Central Patagonia: New evidence and tectonic implications, *Andean Geology*, 37(2), 276-  
682 299, <http://dx.doi.org/10.5027/andgeoV37n2-a02>, 2010.

683 Lagabrielle, Y., Suárez, M., Rossello, E. A., Hérail, G., Martinod, J., Régnier, M., and de la  
684 Cruz, R.: Neogene to Quaternary tectonic evolution of the Patagonian Andes at the latitude of  
685 the Chile Triple Junction, *Tectonophysics*, 385(1-4), 211-241,  
686 <https://doi.org/10.1016/j.tecto.2004.04.023>, 2004.

687 Lange, H., Casassa, G., Ivins, E. R., Schröder, L., Fritsche, M., Richter, A., Groh, A., and  
688 Dietrich, R.: Observed crustal uplift near the Southern Patagonian Icefield constrains  
689 improved viscoelastic Earth models, *Geophysical Research Letters*, 41(3), 805-812,  
690 <https://doi.org/10.1002/2013GL058419>, 2014.

691 Larson, K. M., Bürgmann, R., Bilham, R., and Freymueller, J. T.: Kinematics of the India-  
692 Eurasia collision zone from GPS measurements, *Journal of Geophysical Research: Solid*  
693 *Earth*, 104(B1), 1077-1093, <https://doi.org/10.1029/1998JB900043>, 1999.

694 Lenzano, M. G., Rivera, A., Durand, M., Vacaflor, P., Carbonetti, M., Lannutti, E., Gende,  
695 M., and Lenzano, L.: Detection of Crustal Uplift Deformation in Response to Glacier  
696 Wastage in Southern Patagonia, *Remote Sensing*, 15(3), 584,  
697 <https://doi.org/10.3390/rs15030584>, 2023.

698 Mark, H. F., Wiens, D. A., Ivins, E. R., Richter, A., Ben Mansour, W., Magnani, M. B.,  
699 Marderwald, E., Adaros, R., and Barrientos, S.: Lithospheric erosion in the Patagonian slab  
700 window, and implications for glacial isostasy, *Geophysical Research Letters*, 49(2),  
701 e2021GL096863, <https://doi.org/10.1029/2021GL096863>, 2022.

702 Martinod, J., Pouyaud, B., Carretier, S., Guillaume, B., and Hérail, G.: Geomorphic Records  
703 along the General Carrera (Chile)–Buenos Aires (Argentina) Glacial Lake (46°–48° S),



704 Climate Inferences, and Glacial Rebound for the Past 7–9 ka: A discussion, *The Journal of*  
705 *Geology*, 124(5), 631-635, <https://doi.org/10.1086/687550>, 2016.

706 McCulloch, R. D., Bentley, M. J., Purves, R. S., Hulton, N. R., Sugden, D. E., *and*  
707 Clapperton, C. M.: Climatic inferences from glacial and palaeoecological evidence at the last  
708 glacial termination, southern South America, *Journal of Quaternary Science: Published for*  
709 *the Quaternary Research Association*, 15(4), 409-417, [https://doi.org/10.1002/1099-](https://doi.org/10.1002/1099-1417(200005)15:4<409::AID-JQS539>3.0.CO;2-%23)  
710 [1417\(200005\)15:4<409::AID-JQS539>3.0.CO;2-%23](https://doi.org/10.1002/1099-1417(200005)15:4<409::AID-JQS539>3.0.CO;2-%23), 2000.

711 McCulloch, R. D., Fogwill, C. J., Sugden, D. E., Bentley, M. J., *and* Kubik, P. W.:  
712 Chronology of the last glaciation in central Strait of Magellan and Bahía Inútil, southernmost  
713 South America, *Geografiska Annaler: Series A, Physical Geography*, 87(2), 289-312,  
714 <https://doi.org/10.1111/j.0435-3676.2005.00260.x>, 2005.

715 McKenzie, D. A. N., *and* Bickle, M. J.: The volume and composition of melt generated by  
716 extension of the lithosphere, *Journal of petrology*, 29(3), 625-679,  
717 <https://doi.org/10.1093/petrology/29.3.625>, 1988.

718 McKenzie, D., *and* Richter, F. M.: Parameterized thermal convection in a layered region and  
719 the thermal history of the Earth, *Journal of Geophysical Research: Solid Earth*, 86(B12),  
720 11667-11680, <https://doi.org/10.1029/JB086iB12p11667>, 1981.

721 Millan, R., Rignot, E., Rivera, A., Martineau, V., Mougnot, J., Zamora, R., Uribe, J.,  
722 Lenzano, G., De Fleurian, B., Li, X., Gim, Y., *and* Kirchner, D.: Ice thickness and bed  
723 elevation of the Northern and Southern Patagonian Icefields, *Geophysical Research Letters*,  
724 46(12), 6626-6635, <https://doi.org/10.1029/2019GL082485>, 2019.

725 Mitrovica, J. X., *and* Forte, A.: M. Radial profile of mantle viscosity: Results from the joint  
726 inversion of convection and postglacial rebound observables, *Journal of Geophysical*  
727 *Research: Solid Earth*, 102(B2), 2751-2769, <https://doi.org/10.1029/96JB03175>, 1997.

728 Molnar, P., *and* England, P.: Late Cenozoic uplift of mountain ranges and global climate  
729 change: chicken or egg? *Nature*, 346(6279), 29-34, <https://doi.org/10.1038/346029a0>, 1990.

730 Moreno, P. I., Denton, G. H., Moreno, H., Lowell, T. V., Putnam, A. E., *and* Kaplan, M. R.:  
731 Radiocarbon chronology of the last glacial maximum and its termination in northwestern  
732 Patagonia, *Quaternary Science Reviews*, 122, 233-249,  
733 <https://doi.org/10.1016/j.quascirev.2015.05.027>, 2015.

734 [Moreno, P. I., Denton, G. H., Moreno, H., Lowell, T. V., Putnam, A. E., and Kaplan, M. R.:](https://doi.org/10.1016/j.quascirev.2015.05.027)  
735 [Radiocarbon chronology of the last glacial maximum and its termination in northwestern](https://doi.org/10.1016/j.quascirev.2015.05.027)  
736 [Patagonia, Quaternary Science Reviews, 122, 233-249,](https://doi.org/10.1016/j.quascirev.2015.05.027)  
737 <https://doi.org/10.1016/j.quascirev.2015.05.027>, 2015.

738 Moreno, P. I., Lowell, T. V., Jacobson Jr, G. L., *and* Denton, G. H. Abrupt vegetation and  
739 climate changes during the last glacial maximum and last termination in the Chilean Lake  
740 District: a case study from Canal de la Puntilla (41 S), *Geografiska Annaler: Series A,*  
741 *Physical Geography*, 81(2), 285-311, <https://doi.org/10.1111/1468-0459.00059>, 1999.

742 [Muller, V. A. P., Sue, C., Valla, P., Sternai, P., Simon-Labrie, T., Gautheron, C., Cuffey, K.,](https://doi.org/10.22541/essoar.168332179.93378898/v1)  
743 [Grujic, D., Bernet, M., Martinod, J., Ghiglione, M., Herman, F., Reiners, P., Shuster, D.,](https://doi.org/10.22541/essoar.168332179.93378898/v1)  
744 [Willett, C., Baumgartner, L., and Braun, J.: Geodynamic and climatic forcing on late-](https://doi.org/10.22541/essoar.168332179.93378898/v1)  
745 [Cenozoic exhumation of the Southern Patagonian Andes \(Fitz Roy and Torres del Paine](https://doi.org/10.22541/essoar.168332179.93378898/v1)  
746 [massifs\), Authorea Preprints \[preprint\],](https://doi.org/10.22541/essoar.168332179.93378898/v1)  
747 <https://doi.org/10.22541/essoar.168332179.93378898/v1>, 05 May 2023.

748 Muller, V. A., Calderón, M., Fosdick, J. C., Ghiglione, M. C., Cury, L. F., Massonne, H. J.,

749 | Fanning, M.C., Warren, C.J., Ramírez de Arellano, C., [and](#) Sternai, P.: The closure of the  
750 | Rocas Verdes Basin and early tectono-metamorphic evolution of the Magallanes Fold-and-  
751 | Thrust Belt, southern Patagonian Andes (52–54° S), *Tectonophysics*, 798, 228686,  
752 | <https://doi.org/10.1016/j.tecto.2020.228686>, 2021.

753 | Muller, V. A., Sternai, P., Sue, C., Simon-Labric, T., [and](#) Valla, P. G.: Climatic control on the  
754 | location of continental volcanic arcs, *Scientific Reports*, 12(1), 1-13,  
755 | <https://doi.org/10.1038/s41598-022-26158-2>, 2022.

756 | [Pedoja, K., Regard, V., Husson, L., Martinod, J., Guillaume, B., Fucks, E., Iglesias, M., and](#)  
757 | [Weill, P.:](#) Uplift of Quaternary shorelines in eastern Patagonia: Darwin revisited,  
758 | *Geomorphology*, 127(3-4), 121-142, <https://doi.org/10.1016/j.geomorph.2010.08.003>, 2011.

759 | Peltier, W. R., [and](#) Andrews, J. T.: Glacial-isostatic adjustment—I. The forward problem,  
760 | *Geophysical Journal International*, 46(3), 605-646, [https://doi.org/10.1111/j.1365-](https://doi.org/10.1111/j.1365-246X.1976.tb01251.x)  
761 | [246X.1976.tb01251.x](https://doi.org/10.1111/j.1365-246X.1976.tb01251.x), 1976.

762 | [Peltier, W. R., Argus, D. F., and Drummond, R.:](#) Comment on “An assessment of the ICE-  
763 | [6G\\_C \(VM5a\) glacial isostatic adjustment model”](#) by Purcell et al. *Journal of Geophysical*  
764 | [Research: Solid Earth](#), 123(2), 2019-2028, <https://doi.org/10.1002/2016JB013844>, 2018.

765 | Peltier, W. R.: Global glacial isostasy and the surface of the ice-age Earth: the ICE-5G  
766 | (VM2) model and GRACE, *Annu. Rev. Earth Planet. Sci.*, 32, 111-149,  
767 | <https://doi.org/10.1146/annurev.earth.32.082503.144359>, 2004.

768 | Peltier, W. R.: Mantle viscosity and ice-age ice sheet topography, *Science*, 273(5280), 1359-  
769 | 1364, <https://doi.org/10.1126/science.273.5280.1359>, 1996.

770 | Rabassa, J.: Late cenozoic glaciations in Patagonia and Tierra del Fuego, *Developments in*  
771 | *quaternary sciences*, 11, 151-204, [https://doi.org/10.1016/S1571-0866\(07\)10008-7](https://doi.org/10.1016/S1571-0866(07)10008-7), 2008.

772 | Ramos, V. A., [and](#) Kay, S. M.: Southern Patagonian plateau basalts and deformation: backarc  
773 | testimony of ridge collisions, *Tectonophysics*, 205(1-3), 261-282,  
774 | [https://doi.org/10.1016/0040-1951\(92\)90430-E](https://doi.org/10.1016/0040-1951(92)90430-E), 1992.

775 | Ramos, V. A.: Seismic ridge subduction and topography: Foreland deformation in the  
776 | Patagonian Andes, *Tectonophysics*, 399(1-4), 73-86,  
777 | <https://doi.org/10.1016/j.tecto.2004.12.016>, 2005.

778 | Ranalli, G.: *Rheology of the Earth*, Springer Science & Business Media, [ISBN 0-412-54670-](#)  
779 | [1](#), 1995.

780 | Ranalli, G.: Rheology of the lithosphere in space and time, *Geological Society, London,*  
781 | *Special Publications*, 121(1), 19-37, <https://doi.org/10.1144/GSL.SP.1997.121.01.02>, 1997.

782 | Ravikumar, M., Singh, B., Pavan Kumar, V., Satyakumar, A. V., Ramesh, D. S., [and](#) Tiwari,  
783 | V. M.: Lithospheric density structure and effective elastic thickness beneath Himalaya and  
784 | Tibetan Plateau: Inference from the integrated analysis of gravity, geoid, and topographic  
785 | data incorporating seismic constraints, *Tectonics*, 39(10), e2020TC006219,  
786 | <https://doi.org/10.1029/2020TC006219>, 2020.

787 | [Reynhout, S. A., Sagredo, E. A., Kaplan, M. R., Aravena, J. C., Martini, M. A., Moreno, P. I.,](#)  
788 | [Rojas, M., Schwartz, R., and Schaefer, J. M.:](#) Holocene glacier fluctuations in Patagonia are  
789 | [modulated by summer insolation intensity and paced by Southern Annular Mode-like](#)  
790 | [variability](#), *Quaternary Science Reviews*, 220, 178-187,  
791 | <https://doi.org/10.1016/j.quascirev.2019.05.029>, 2019.

792 | [Richter, A., Ivins, E., Lange, H., Mendoza, L., Schröder, L., Hormaechea, J. L., Casassa, G.,](#)

793 [Marderwald, E., Fritsche, M., Perdomo, R., Horwath, M., and Dietrich, R.: Crustal](#)  
794 [deformation across the Southern Patagonian Icefield observed by GNSS, Earth and Planetary](#)  
795 [Science Letters, 452, 206-215, <https://doi.org/10.1016/j.epsl.2016.07.042>, 2016.](#)

796 [Rignot, E., Rivera, A., and Casassa, G.: Contribution of the Patagonia Icefields of South](#)  
797 [America to sea level rise, Science, 302\(5644\), 434-437,](#)  
798 <https://doi.org/10.1126/science.1087393>, 2003.

799 [Robertson Maurice, S. D., Wiens, D. A., Koper, K. D., and Vera, E. Crustal and upper mantle](#)  
800 [structure of southernmost South America inferred from regional waveform inversion, Journal](#)  
801 [of Geophysical Research: Solid Earth, 108\(B1\), <https://doi.org/10.1029/2002JB001828>,](#)  
802 [2003.](https://doi.org/10.1029/2002JB001828)

803 [Ruddiman, W. F., Raymo, M., and McIntyre, A.: Matuyama 41,000-year cycles: North](#)  
804 [Atlantic Ocean and northern hemisphere ice sheets, Earth and Planetary Science Letters,](#)  
805 [80\(1-2\), 117-129, \[https://doi.org/10.1016/0012-821X\\(86\\)90024-5\]\(https://doi.org/10.1016/0012-821X\(86\)90024-5\), 1986.](#)

806 [Russo, R. M., Gallego, A., Comte, D., Mocanu, V. I., Murdie, R. E., and VanDecar, J. C.:](#)  
807 [Source-side shear wave splitting and upper mantle flow in the Chile Ridge subduction region,](#)  
808 [Geology, 38\(8\), 707-710, <https://doi.org/10.1130/G30920.1>, 2010.](#)

809 [Russo, R. M., Luo, H., Wang, K., Ambrosius, B., Mocanu, V., He, J., James, T., Bevis, M.,](#)  
810 [and Fernandes, R.: Lateral variation in slab window viscosity inferred from global navigation](#)  
811 [satellite system \(GNSS\)-observed uplift due to recent mass loss at Patagonia ice fields,](#)  
812 [Geology, 50\(1\), 111-115, <https://doi.org/10.1130/G49388.1>, 2022.](#)

813 [Scalabrino, B., Lagabrielle, Y., Malavieille, J., Dominguez, S., Melnick, D., Espinoza, F.,](#)  
814 [Suárez, M., and Rossello, E.: A morphotectonic analysis of central Patagonian Cordillera:](#)  
815 [Negative inversion of the Andean belt over a buried spreading center? Tectonics, 29\(2\),](#)  
816 <https://doi.org/10.1029/2009TC002453>, 2010.

817 [Seltzer, A. M., Ng, J., Aeschbach, W., Kipfer, R., Kulongoski, J. T., Severinghaus, J. P., and](#)  
818 [Stute, M.: Widespread six degrees Celsius cooling on land during the Last Glacial Maximum,](#)  
819 [Nature, 593\(7858\), 228-232, <https://doi.org/10.1038/s41586-021-03467-6>, 2021.](#)

820 [Serpelloni, E., Faccenna, C., Spada, G., Dong, D., and Williams, S. D.: Vertical GPS ground](#)  
821 [motion rates in the Euro-Mediterranean region: New evidence of velocity gradients at](#)  
822 [different spatial scales along the Nubia-Eurasia plate boundary, Journal of Geophysical](#)  
823 [Research: Solid Earth, 118\(11\), 6003-6024, <https://doi.org/10.1002/2013JB010102>, 2013.](#)

824 [Stern, C. R., and Kilian, R.: Role of the subducted slab, mantle wedge and continental crust](#)  
825 [in the generation of adakites from the Andean Austral Volcanic Zone, Contributions to](#)  
826 [mineralogy and petrology, 123, 263-281, <https://doi.org/10.1002/2013JB010102>, 1996.](#)

827 [Sternai P., Avouac J.-P., Jolivet L., Faccenna C., Gerya T.V., Becker T., and Menant, A.: On](#)  
828 [the influence of the asthenospheric flow on the tectonics and topography at collision-](#)  
829 [subduction transition zones: comparison with the eastern Tibetan margin, Journal of](#)  
830 [Geodynamics, 100, 18-194, <https://doi.org/10.1016/j.jog.2016.02.009>, 2016b.](#)

831 [Sternai P., Caricchi L., Castelltort S., and Champagnac J.-D.: Deglaciation and glacial](#)  
832 [erosion: a joint control on the magma productivity by continental unloading, Geophysical](#)  
833 [Research Letters, <https://doi.org/10.1002/2015GL067285>, 2016a.](#)

834 [Sternai, P., Muller, V. A. P., Jolivet, L., Garzanti, E., Corti, G., Pasquero, C., Sembroni, A.,](#)  
835 [and Faccenna, C.: Effects of asthenospheric flow and orographic precipitation on continental](#)  
836 [rifting, Tectonophysics, 820, 229120, <https://doi.org/10.1016/j.tecto.2021.229120>, 2021.](#)

837 [Sternai, P., Sue, C., Husson, L., Serpelloni, E., Becker, T. W., Willett, S. D., Faccenna, C., Di](#)

838 Giulio, A., Spada, G., Jolivet, L., Valla, P., Petit, C., Nocquet, J.-M., Walpersdorf, A., and  
839 Castelltort, S.: Present-day uplift of the European Alps: Evaluating mechanisms and models  
840 of their relative contributions, *Earth-Science Reviews*, 190, 589-604,  
841 <https://doi.org/10.1016/j.earscirev.2019.01.005>, 2019.

842 Sternai, P.: Feedbacks between internal and external Earth dynamics, in: *Dynamics of Plate*  
843 *Tectonics and Mantle Convection*, edited by Duarte, J., Elsevier, (pp. 271-294), ISBN 978-0-  
844 [323-85733-8](https://doi.org/10.1016/j.earscirev.2019.01.005), 2023.

845 Sternai, P.: Surface processes forcing on extensional rock melting, *Scientific reports*, 10(1),  
846 1-13, <https://doi.org/10.1038/s41598-020-63920-w>, 2020.

847 Stevens Goddard, A. L., and Fosdick, J. C.: Multichronometer thermochronologic modeling  
848 of migrating spreading ridge subduction in southern Patagonia, *Geology*, 47(6), 555-558,  
849 <https://doi.org/10.1130/G46091.1>, 2019.

850 Strelin, J. A., Kaplan, M. R., Vandergoes, M. J., Denton, G. H., and Schaefer, J. M.:  
851 Holocene glacier history of the Lago Argentino basin, southern Patagonian Icefield,  
852 Quaternary Science Reviews, 101, 124-145, <https://doi.org/10.1016/j.quascirev.2014.06.026>,  
853 2014.

854 Stuhne, G. R., and Peltier, W. R.: Reconciling the ICE-6G\_C reconstruction of glacial  
855 chronology with ice sheet dynamics: The cases of Greenland and Antarctica, *Journal of*  
856 *Geophysical Research: Earth Surface*, 120(9), 1841-1865,  
857 <https://doi.org/10.1002/2015JF003580>, 2015.

858 Sue, C., Delacou, B., Champagnac, J. D., Allanic, C., and Burkhard, M. Aseismic  
859 deformation in the Alps: GPS vs. seismic strain quantification, *Terra Nova*, 19(3), 182-188,  
860 <https://doi.org/10.1111/j.1365-3121.2007.00732.x>, 2007.

861 Sugden, D. E., Hulton, N. R., and Purves, R. S.: Modelling the inception of the Patagonian  
862 icesheet, *Quaternary International*, 95, 55-64, [https://doi.org/10.1016/S1040-6182\(02\)00027-](https://doi.org/10.1016/S1040-6182(02)00027-7)  
863 [7](https://doi.org/10.1016/S1040-6182(02)00027-7), 2002.

864 Thomson, S. N., Brandon, M. T., Tomkin, J. H., Reiners, P. W., Vásquez, C., and Wilson, N.  
865 J.: Glaciation as a destructive and constructive control on mountain building, *Nature*,  
866 467(7313), 313-317, <https://doi.org/10.1038/nature09365>, 2010.

867 Thorndycraft, V. R., Bendle, J. M., Benito, G., Davies, B. J., Sancho, C., Palmer, A. P.,  
868 Fabel, D., Medialdea, A., and Martin, J. R.: Glacial lake evolution and Atlantic-Pacific  
869 drainage reversals during deglaciation of the Patagonian Ice Sheet, *Quaternary Science*  
870 *Reviews*, 203, 102-127, <https://doi.org/10.1016/j.quascirev.2018.10.036>, 2019.

871 Turcotte, D. L., and Schubert, G.: *Geodynamics*, Cambridge university press, ISBN 978-0-  
872 [521-66186-7](https://doi.org/10.1016/j.earscirev.2019.01.005), 2002.

873 Valla, P. G., van der Beek, P. A., Shuster, D. L., Braun, J., Herman, F., Tassan-Got, L., and  
874 Gautheron, C.: Late Neogene exhumation and relief development of the Aar and Aiguilles  
875 Rouges massifs (Swiss Alps) from low-temperature thermochronology modeling and  
876 4He/3He thermochronometry, *Journal of Geophysical Research: Earth Surface*, 117(F1),  
877 <https://doi.org/10.1029/2011JF002043>, 2012.

878 Van der Meijde, M., Julià, J., and Assumpção, M.: Gravity derived moho for south America,  
879 *Tectonophysics*, 609, 456-467, <https://doi.org/10.1016/j.tecto.2013.03.023>, 2013

880 van der Wal, W., Whitehouse, P. L., and Schrama, E. J.: Effect of GIA models with 3D  
881 composite mantle viscosity on GRACE mass balance estimates for Antarctica, *Earth and*

882 | Planetary Science Letters, 414, 134-143, <https://doi.org/10.1016/j.epsl.2015.01.001>, 2015.

883 | Walpersdorf, A., Sue, C., Baize, S., Cotte, N., Bascou, P., Beauval, C., Collard, P., Daniel, G.,  
884 | Dyer, H., Grasso, J.-R., Hautecoeur, O., Helmstetter, A., Hok, S., Langlais, M., Menard, G.,  
885 | Mousavi, Z., Ponton, F., Rizza, M., Rolland, L., Souami, D., and Martinod, J.: Coherence  
886 | between geodetic and seismic deformation in a context of slow tectonic activity (SW Alps,  
887 | France), Journal of Geodynamics, 85, 58-65, <https://doi.org/10.1016/j.jog.2015.02.001>, 2015.

888 | Watts, A. B.: Isostasy and Flexure of the Lithosphere, Cambridge University Press, [ISBN 0-  
889 | 521-62272](https://doi.org/10.1017/9780521622720), 2001.

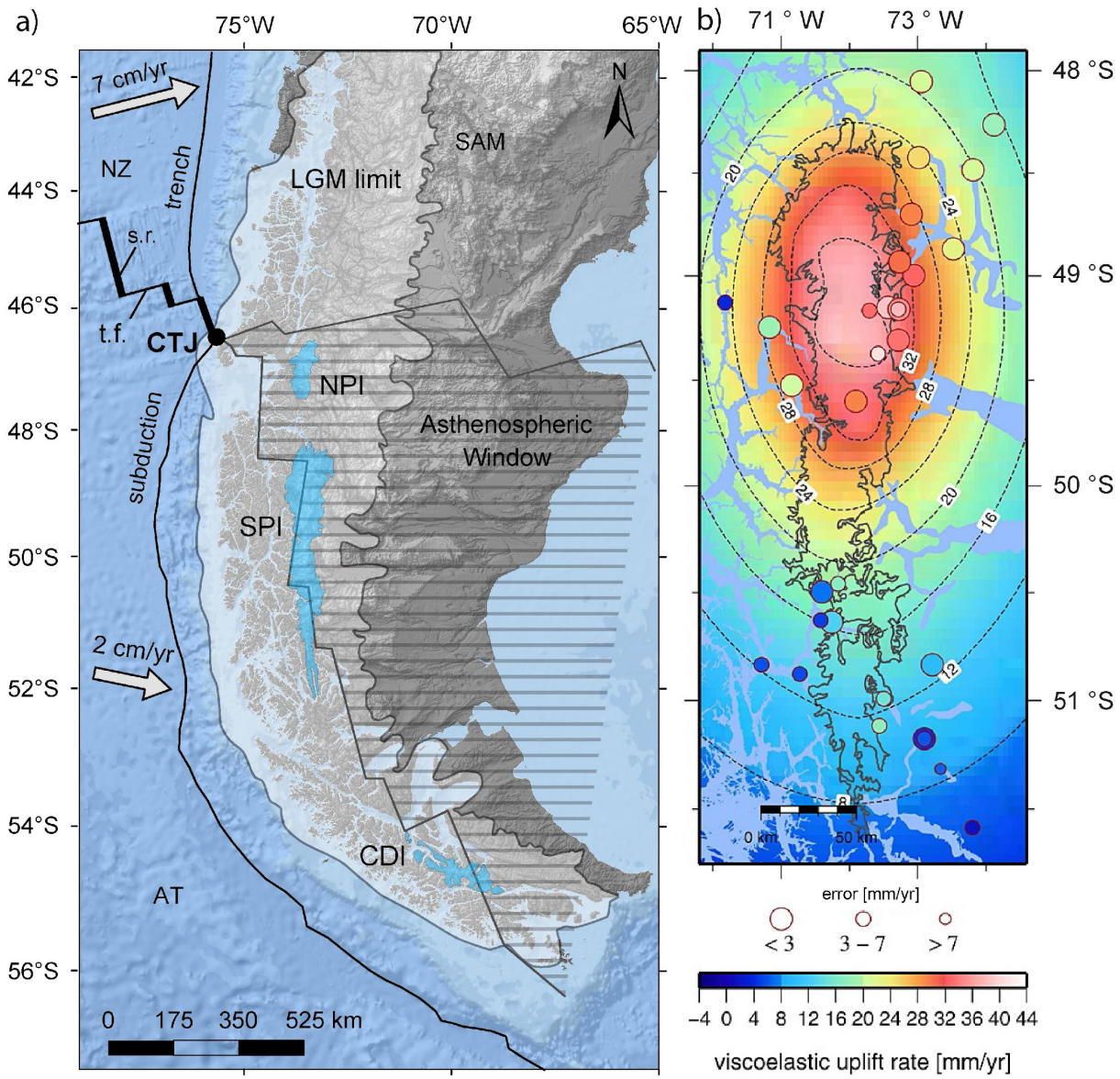
890 | [Whitehouse, P. L.: Glacial isostatic adjustment modelling: historical perspectives, recent  
891 | advances, and future directions, Earth surface dynamics, 6\(2\), 401-429,  
892 | https://doi.org/10.5194/esurf-6-401-2018](https://doi.org/10.5194/esurf-6-401-2018), 2018.

893 | Willis, M. J., Melkonian, A. K., Pritchard, M. E., and Rivera, A.: Ice loss from the Southern  
894 | Patagonian ice field, South America, between 2000 and 2012, Geophysical Research Letters,  
895 | 39(17), <https://doi.org/10.1029/2012GL053136>, 2012.

896 | [Yan, Q., Wei, T., and Zhang, Z.: Modeling the climate sensitivity of Patagonian glaciers and  
897 | their responses to climatic change during the global last glacial maximum, Quaternary  
898 | Science Reviews, 288, 107582, https://doi.org/10.1016/j.quascirev.2022.107582](https://doi.org/10.1016/j.quascirev.2022.107582), 2022.

899 |

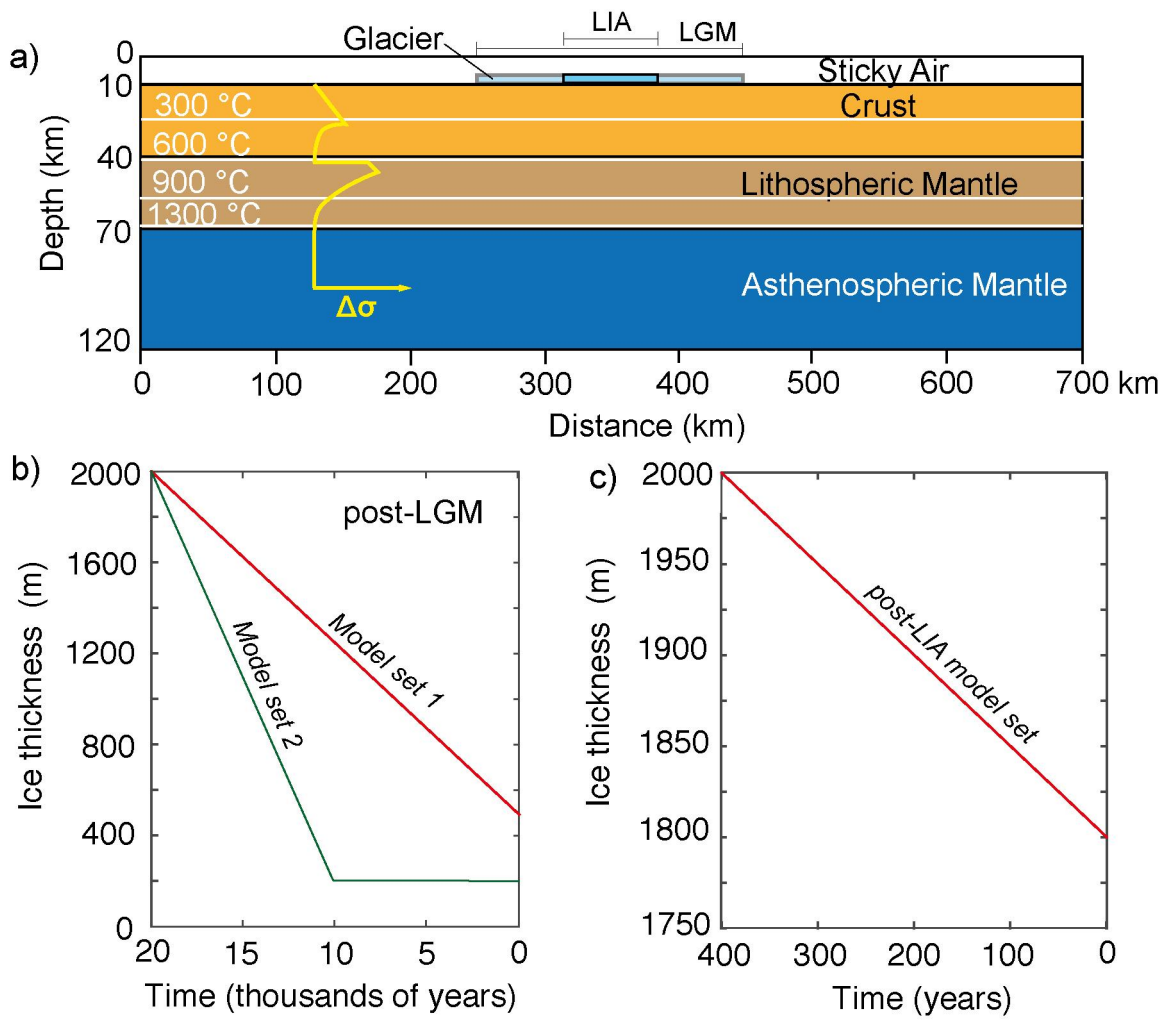




00  
01  
02  
03  
04  
05  
06  
07  
08

**Fig. 1. Regional context and uplift rate data.** a) Map of southern Patagonia with the Southern Patagonian Icefield (SPI), Northern Patagonian Icefield (NPI), and the Cordillera Darwin Icefield (CDI) in light blue, the approximate extension of the Patagonian Ice Sheet at the Last Glacial Maximum (LGM) ([adapted from Thorndycraft et al., 2019](#)), and the approximate extension of the present-day asthenospheric window (dashed region) beneath the South American Continent (SAM) ([adapted from Breitsprecher and Thorkelson, 2009](#)). In the Pacific Ocean, the spreading ridges (s.r., thick black lines) and transform faults (t.f., thin black lines) separate the Nazca (NZ) and the Antarctic (AT) plates. The subduction trench is also highlighted in black. The arrows show the approximate rate and direction of subduction of the oceanic plates ([adapted from DeMets et al., 2010](#)). b) Zoom on the SPI with GNSS-measured rock uplift rates ([color-coded disks](#)) used to estimate the viscoelastic uplift rates [in](#) Lange et al. (2014).





09

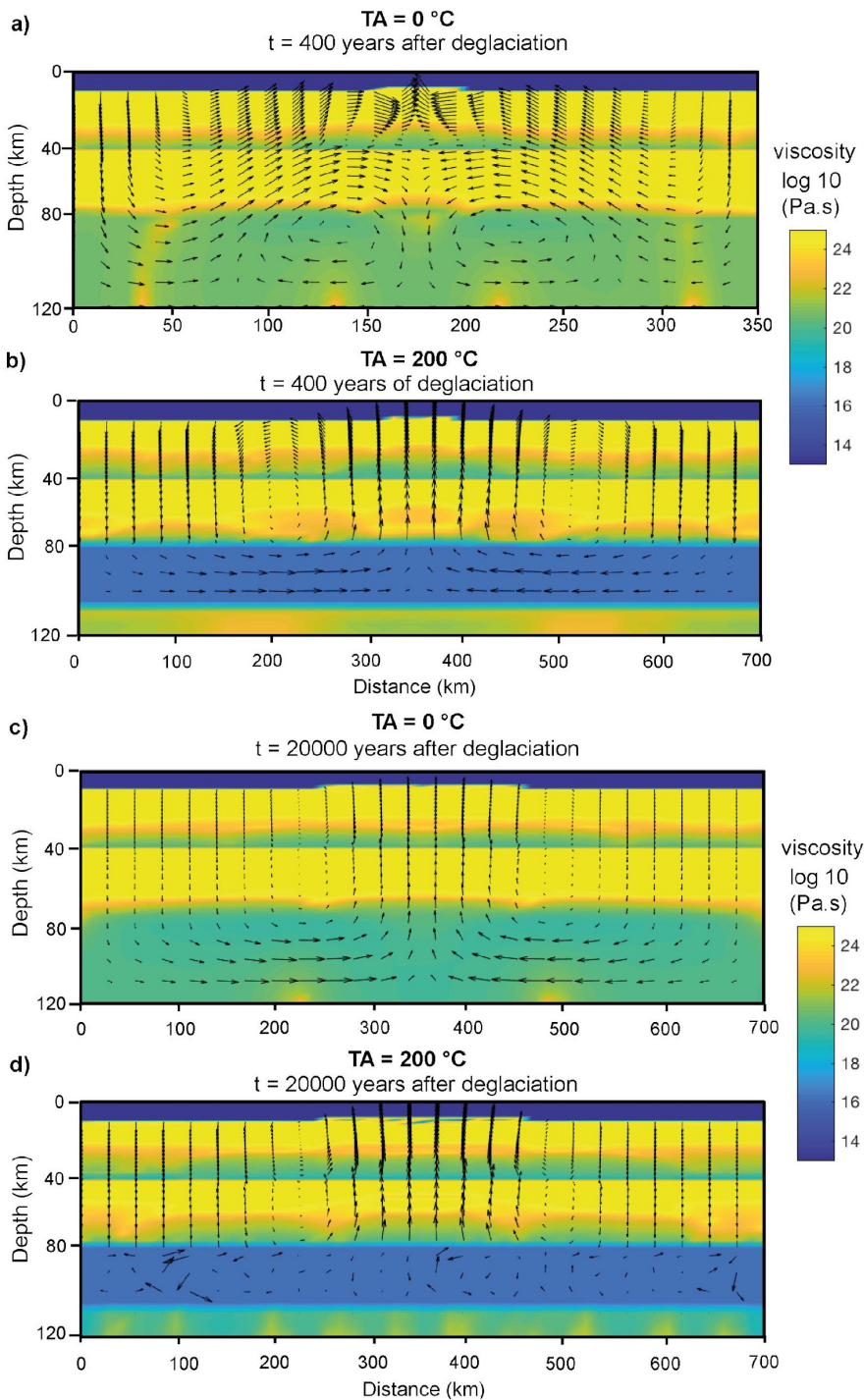
10

11

12

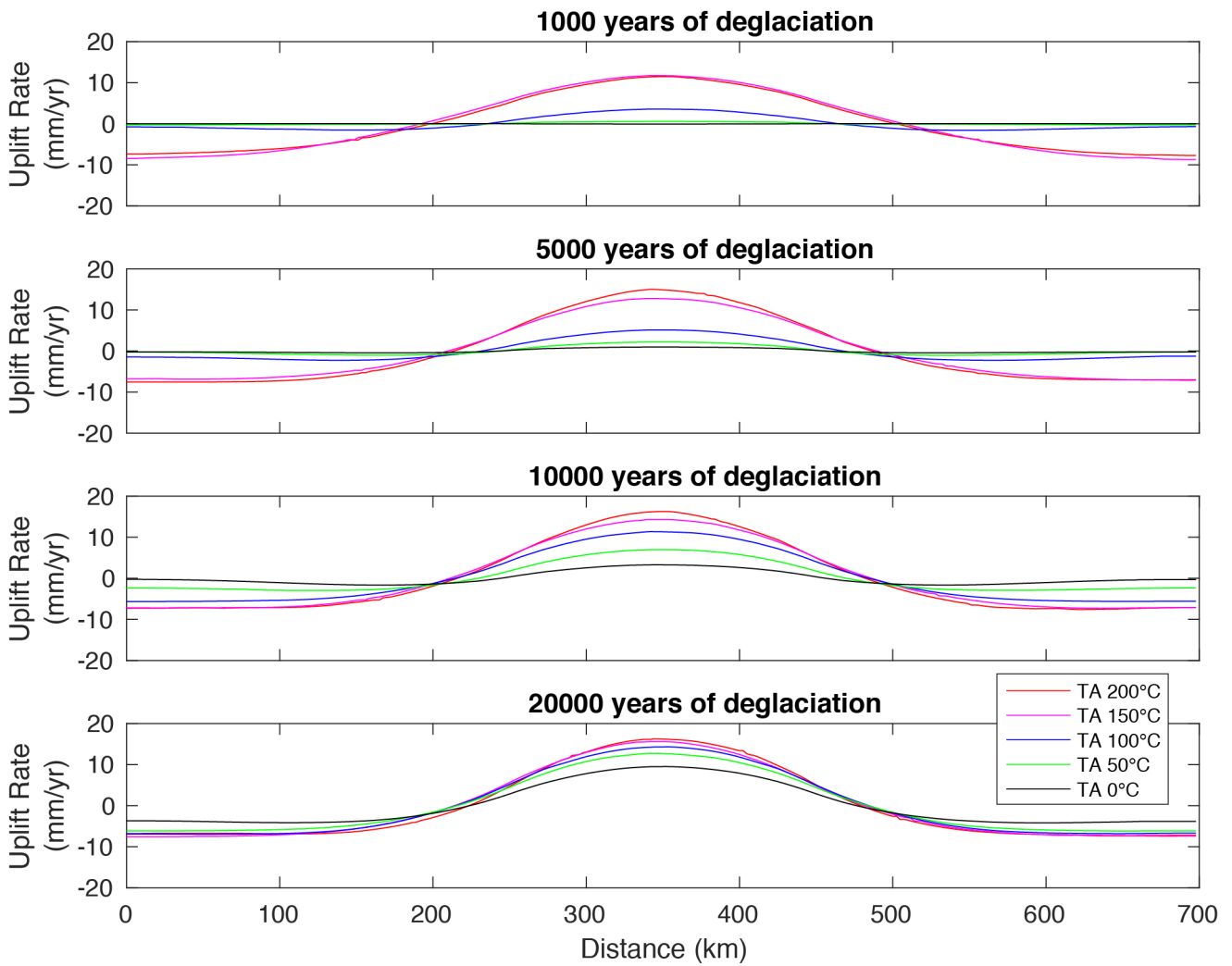
13

**Fig. 2. Reference numerical model setup.** a) Thermo-mechanical numerical model domain with rheological layers (Table 1), isotherms (white lines), and yield strength ( $\Delta\sigma = \sigma_1 - \sigma_3$ ) profile (yellow line). The yield strength ( $\Delta\sigma$ ) profile is not scaled and aims to show the proportionality of the yield strength amongst the layers, dependent on the temperature and composition (Eq. 4). (b, c) Ice thickness vs. time used in the numerical models to simulate the post-LGM deglaciation in two model sets (b), and the post-LIA deglaciation (c).



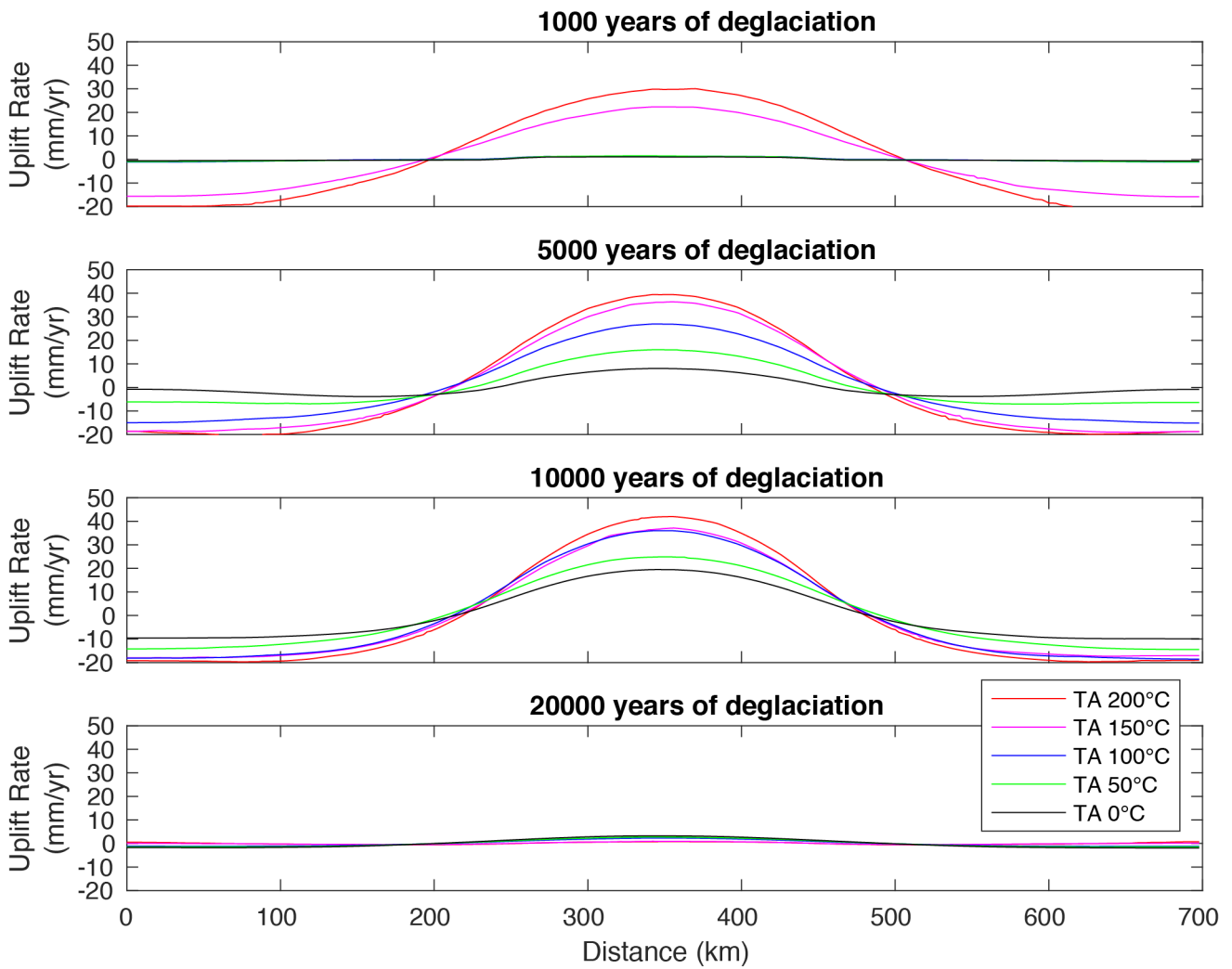
14  
15  
16  
17  
18  
19  
20  
21

**Fig. 3. Distribution of viscosity and velocity vectors in the numerical models.** *a, c*) Reference model without an asthenospheric thermal anomaly,  $TA = 0\text{ }^{\circ}\text{C}$ , in the last timestep of post-LIA deglaciation (a) and of Model set 1 of post-LGM deglaciation (c). *b, d*) Model with the higher simulated asthenospheric thermal anomaly,  $TA = 200\text{ }^{\circ}\text{C}$ , in the last timestep of post-LIA deglaciation (b) and of Model set 1 of post-LGM deglaciation. Model set 2 has a very similar viscosity and velocity vectors distribution with Model set 1 in the last deglaciation timestep. Velocity vectors do not have the same scaling and are only meant for visualization purpose.



22  
23  
24  
25

**Fig. 4. Surface uplift rates vs. distance for Model set 1 of post-LGM deglaciation.** a)  $t = 1000$  years of deglaciation, b)  $t = 5000$  years of deglaciation, c)  $t = 10000$  of deglaciation, d) 20000 years of deglaciation. Different line colours correspond to different TA.



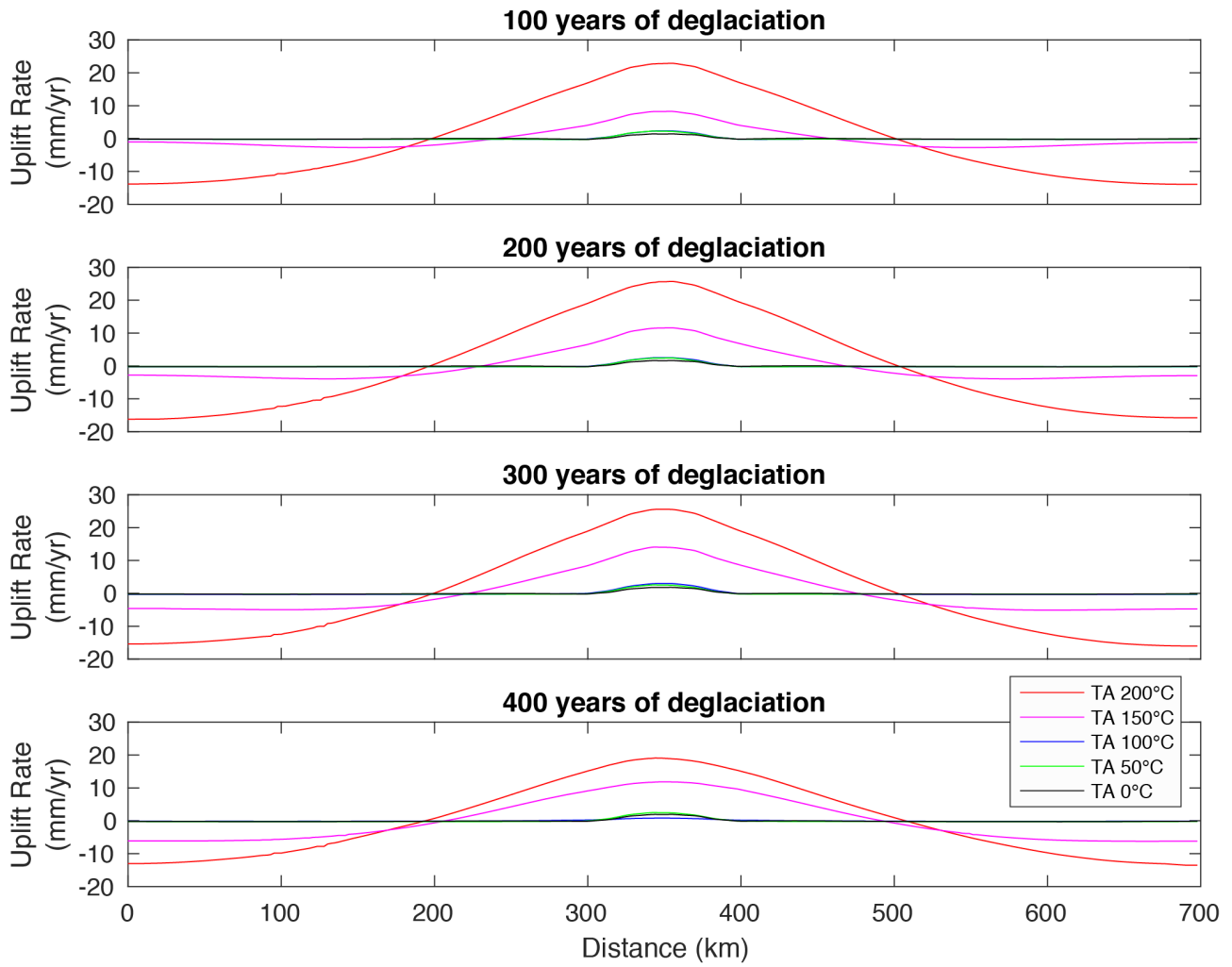
26

27

28

29

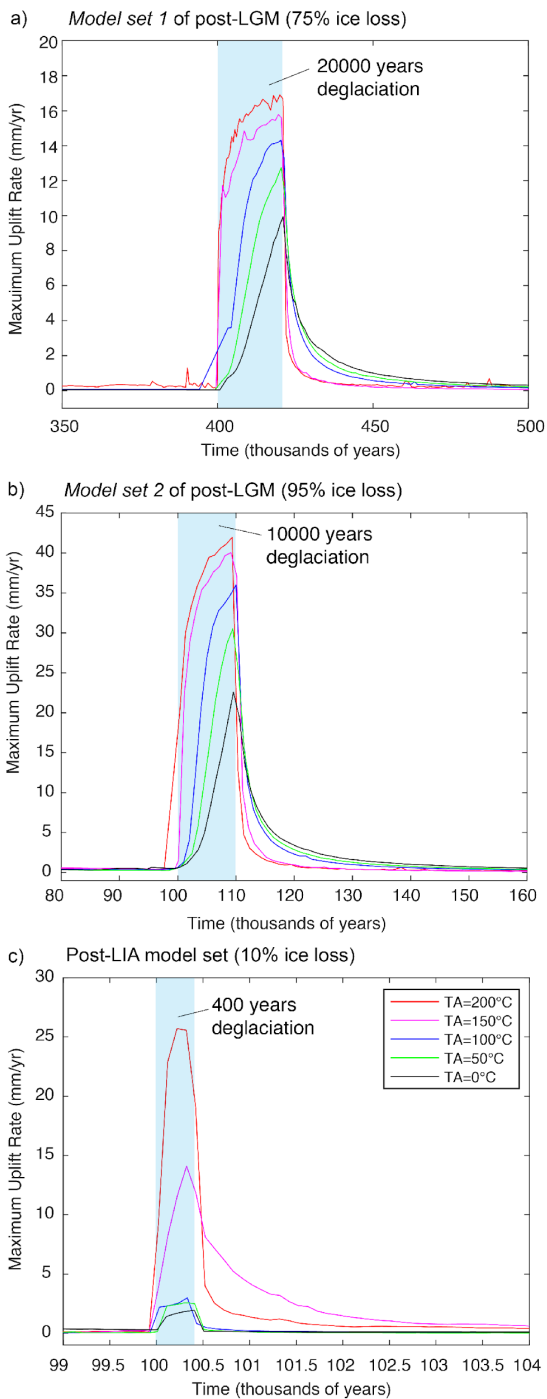
**Fig. 5. Surface uplift rates vs. distance for *Model set 2* of post-LGM deglaciation. a)  $t = 1000$  years of deglaciation, b)  $t = 5000$  years of deglaciation, c)  $t = 10000$  of deglaciation, d) 20000 years of deglaciation. Different line colours correspond to different TA.**



30  
31  
32

**Fig. 6. Surface uplift rates vs. distance for post-LIA deglaciation model set.** a)  $t = 100$  years of deglaciation, b)  $t = 200$  years of deglaciation, c)  $t = 300$  years of deglaciation, d) 400 years of deglaciation. Different line colours correspond to different TA.





33

34

35

36

37

38

**Fig. 7. Maximum uplift rates vs. time for model sets of deglaciation with different TA.** a) *Model set 1* of post-LGM deglaciation accounting of 75% of ice loss in 20000 years, deglaciation starts at 400000 years. b) *Model set 2* of post-LGM deglaciation accounting of 95% of ice loss in 10000 years, deglaciation starts at 100000 years and c) Post-LIA deglaciation model set accounting 10% of ice loss in 400 years (blue-shaded region), deglaciation starts at 100000 years. Blue-shaded regions highlight the modelled deglaciation intervals. Please note that the time axis in a, b, and c are different and post-LGM models account for longer timescales.

39 **Table 1** – Material properties used in the numerical experiments.

	$\rho_0^s$ (km/m <sup>3</sup> )	$E_a$ (kJ/mol)	$V_a$ (m <sup>3</sup> /mol)	$n$	$C$ (Mpa)	$Visc.$ flow law	$Sin$ ( $\phi_{eff}$ )	$c$ (W/m/K)	$\mu$ (Gpa)	$C_p$ (J/kg/K)	$H_r$ ( $\mu$ W/m <sup>3</sup> )	$H_l$ (kJ/kg)	$\alpha$ (1/k)	$\beta$ (1/Pa)
<b>Crust</b>	2800	154	0	2.3	10	Wet Qz.	0.2	$0.64+807/(T+77)$	10	1000	1	300	$3 \times 10^{-5}$	$1 \times 10^{-11}$
<b>Lithospheric mantle</b>	3250	532	10	3.5	10	Dry Ol.	0.6	$0.73+1293/(T+77)$	67	1000	0.022	400	$3 \times 10^{-5}$	$1 \times 10^{-11}$
<b>Asthenospheric mantle</b>	3250	532	10	3.5	10	Dry Ol.	0.6	$0.73+1293/(T+77)$	67	1000	0.022	400	$3 \times 10^{-5}$	$1 \times 10^{-11}$
<b>Ice</b>	920	154	0	2.3	10	-	0	$0.73+1293/(T+77)$	67	1000	0.022	400	$3 \times 10^{-5}$	$1 \times 10^{-11}$

40  $\rho_0^s$  is the standard densities of solid rocks;  $E_a$  is the activation energy;  $V_a$  is the activation volume;  $n$  is the stress exponent;  $C$  is cohesion;  
 41  $\phi_{eff}$  is the effective internal friction angle;  $c$  is thermal conductivity;  $\mu$  is the shear modulus;  $C_p$  is the specific heat capacity;  $H_r$  and  $H_l$   
 42 are the radiogenic and latent heat productions, respectively;  $\alpha$  is thermal expansion;  $\beta$  is compressibility. Qz and Ol are quartzite and  
 43 olivine, respectively. All rheological and partial melting laws/parameters are based on experimental rock mechanics and petrology  
 44 (Ranalli, 1995; Hirschmann, 2000; Johannes, 1985; Turcotte and Schubert, 2002).  
 45

46  
47  
48  
49  
50

**Table 2 – Maximum uplift rates derived from the numerical models with a thermal anomaly (TA) of 0, 50, 100, 150 and 200 °C for the Model set 1 (a) and Model set 2 (b) of post-LGM deglaciation, and the post-LIA deglaciation model set (c). The t = 0 is the timestep immediately before the beginning of deglaciation, and other selected timesteps show how the uplift rates change during the deglaciation until it is over for the post-LGM (a,b) and post-LIA (c) deglaciation intervals. Fig. 7 is a plot of the maximum uplift rate vs. time calculated for each timestep in all numerical models.**

<b>a) Model set 1 of post-LGM deglaciation (20000 years)</b>							
TA (°C)	Maximum uplift rate (mm/yr)						
0	0.04	0.04	0.98	3.28	6.43	9.50	4.98
50	0.05	0.56	2.21	6.10	10.76	12.75	4.66
100	0.07	3.58	5.14	11.37	13.63	14.31	4.07
150	0.05	11.72	12.79	14.32	15.18	15.59	1.39
200	0.15	11.48	15.02	16.26	16.46	16.26	0.90
	t = 0	t = 1000 yr	t = 5000 yr	t = 10000 yr	t = 15000 yr	t = 20000 yr	t = 25000 yr
<b>b) Model set 2 of post-LGM deglaciation (10000 years)</b>							
TA (°C)	Maximum uplift rate (mm/yr)						
0	0.50	1.09	8.03	19.48	5.69	3.12	2.15
50	0.25	1.52	15.93	24.87	5.24	2.72	1.73
100	0.33	1.29	26.94	36.02	4.94	2.30	1.41
150	0.43	22.30	36.33	37.11	1.93	0.93	0.60
200	0.37	30.05	39.46	41.98	1.48	0.75	0.50
	t = 0	t = 1000 yr	t = 5000 yr	t = 10000 yr	t = 15000 yr	t = 20000 yr	t = 25000 yr
<b>c) post-LIA deglaciation model set (400 years)</b>							
TA (°C)	Maximum uplift rate (mm/yr)						
0	0.43	1.412	1.67	1.84	1.95	0.18	0.10
50	0.03	2.28	2.43	2.57	2.45	0.30	0.23
100	0.03	2.20	2.32	2.52	2.99	0.49	0.38
150	0.09	8.27	11.57	14.03	11.83	8.11	7.15
200	0.10	22.89	25.70	25.57	18.97	4.00	2.55
	t = 0	t = 100 yr	t = 200 yr	t = 300 yr	t = 400 yr	t = 500 yr	t = 600 yr

51